INTERNATIONAL JOURNAL FOR NUMERICAL METHODS IN FLUIDS
Int. J. Numer. Meth. Fluids 2008; **56**:419–452

A robust high-resolution finite volume scheme for the simulation of long waves over complex domains

A. I. Delis[1, 2, *, †], M. Kazolea[1, 2] and N. A. Kampanis[2]

[1] *Department of Sciences, Division of Mathematics, Technical University of Crete, University Campus,*
Chania 73100, Crete, Greece
[2] *Institute of Applied and Computational Mathematics, Foundation for Research and Technology Hellas-FORTH,*
P.O. Box 1385, Heraklion 71110, Crete, Greece

SUMMARY

The propagation, runup and rundown of long surface waves are numerically investigated, initially in one dimension, using a well-balanced high-resolution finite volume scheme. A conservative form of the nonlinear shallow water equations with source terms is solved numerically using a high-resolution Godunov-type explicit scheme coupled with Roe's approximate Riemann solver. The scheme is also extended to handle two-dimensional complex domains. The numerical difficulties related to the presence of the topography source terms in the model equations along with the appearance of the wet/dry fronts are properly treated and extended. The resulting numerical model accurately describes breaking waves as bores or hydraulic jumps and conserves volume across flow discontinuities. Numerical results show very good agreement with previously presented analytical or asymptotic solutions as well as with experimental benchmark data. Copyright © 2007 John Wiley & Sons, Ltd.

Received 30 November 2006; Revised 19 March 2007; Accepted 6 May 2007

KEY WORDS: long waves; wave breaking; wave runup and rundown; shallow water equations; finite volume; wet/dry fronts

1. INTRODUCTION

Shallow water long waves, such as tides, tsunamis and storm surges, can develop large amplitudes in coastal waters with the (hazardous) potential for causing casualties and large property damage. A considerable research effort has been devoted in recent years to the development of various analytical and numerical models based on the depth-integrated, nonlinear shallow water equations

---

*Correspondence to: A. I. Delis, Department of Sciences, Division of Mathematics, Technical University of Crete, University Campus, Chania 73100, Crete, Greece.

†E-mail: adelis@science.tuc.gr

(NLSW) in order to describe the physical process. The analytical approaches provide exact solutions for idealized situations (e.g. nonbreaking wave propagation and runup) but offer insights into the physical process, see for example [1–5]. However, due to the complex nature of the water motion, especially during the process of wave breaking, any simulation models of the runup of breaking long waves must be treated numerically. Numerical models can provide approximate solutions in more general settings suitable for practical applications as predictive tools.

The NLSW equations have been employed widely to model wave propagation and runup, see for example [6–14] among others. As it was stressed out in [6, 9], the analogy between a shallow water breaking wave and a shock wave in gas dynamics suggests that if provision is made in a numerical model of the NLSW equations to account for the energy dissipation associated with wave breaking, these equations may also be used to simulate the runup of breaking waves. In this case the post-breaking condition can be simplified and represented as a propagating bore (a shock discontinuity). In general, the models utilizing the NLSW equations although having limitations, such as failing to provide depthwise variations in velocity and omit dispersive effects, appear to be able to model important aspects of the wave breaking process and the general characteristics of the runup process. The main computational challenges are the treatment of the wet/dry fronts in the presence of topography, which correspond to a moving shoreline, and the calculation of discontinuities. As a long or very long wave approaches shallow water its wavelength and energy are compressed and its amplitude increase. In this region nonlinearities lead to steepening waves, propagating bores or even breaking waves. Only the most general valid integral form of the NLSW equations is valid near discontinuities and modelling this regime accurately requires a numerical model that can correctly compute steep gradients and discontinuities.

Finite difference schemes have been commonly used in one- and two-dimensional long wave runup models solving, usually, the nonconservative (primitive) form of the NLSW equations. Titov and Synolakis [6] solved the characteristic form of the NLSW equations using finite difference methods and, in [8], extended their one-dimensional model to two dimensions through a splitting scheme and used a Neumann-type technique to extrapolate the water line velocity. Liu *et al.* [7] modelled the runup through flooding and drying on the computational cells in response to adjacent water level changes. For reviews on finite difference methods please refer also to [15, 16].

When dealing with flow discontinuities, volume conservation becomes an important issue for schemes based on nonconservative differential form of the NLSW equations. The finite volume method, however, has the advantage of solving the integral form of the nonlinear equations as a fully conservative scheme. The Godunov-type formulation with a Riemann solver has such good shock capturing capability. Dodd [10] investigated one-dimensional wave runup, overtopping and regeneration problems using a Roe-type Riemann solver and resolved the moving shoreline problem by imposing a minimum water depth in the dry area. Later, Hubbard and Dodd [11] extended the model to two dimensions using an adaptive mesh refinement algorithm. A similar scheme was presented by Bradford and Sanders [17] but used a characteristic method to track the shoreline. Hu *et al.* [13] presented a similar one-dimensional Godunov-type upwind scheme by applying the HLL approximate Riemann solver and by modifying the wave speed on the dry side of a cell interface, thus providing a robust technique to track the moving shoreline. Brocchini *et al.* [18] applied the finite volume method to two dimensions using the WAF method for the exact Riemann problem and treated the moving shoreline as a cavitation problem. Li and Raichelen [9] solved the NLSW equations in one dimension by a WENO scheme and used a computational domain mapping technique to model the shoreline movement. More recently, Leveque and George [14] utilized Leveque's wave-propagation algorithm, a Godunov-type high-resolution finite volume

DOI: 10.1002/fld

method, with a Roe-type Riemann solver that uses the HLLE speeds to handle source terms and dry states.

Other numerical models such as the Boussinesq-type models have been used to simulate wave breaking and runup and up to the point of breaking can represent the nonlinear and dispersive effects to high degree of accuracy. However, a special term has to be included in the momentum conservation equation to account for the dissipation associated with wave breaking. This term must incorporate coefficients that need to be calibrated by field or experimental data, which limit their application. Occasionally, numerical solutions of the Navier–Stokes equations also have been used in wave breaking and runup investigations. However, simple elliptic equations must be solved for the incompressible internal flow, with appropriate boundary conditions for the free surface, which are often too expensive computationally. The finite element method, owing its flexible meshing scheme, is another popular modelling approach in two dimensions. Gopalakrishnan and Tung [19] and Zelt [20] developed long wave runup models based on Eulerian and Langrangian schemes, respectively. For reviews on the mathematical and numerical models please refer to [15, 21, 22] and references therein.

The primary goals of the present study are (a) to apply and extend in high resolution and in two-dimensional complex domains a specific treatment for calculating wet/dry fronts in a well-known finite volume Roe-type scheme; (b) to asses the ability of the numerical scheme to track the moving shoreline line and to (conservatively) capture discontinuities associated with bores or breaking waves, which are essential for runup calculations and (c) to compare the computed results with analytical solutions and, more importantly, to experimental benchmark data. We note here that using the NLSW equations solved by a finite volume scheme for the calculation of the breaking and runup of long waves was not a very common practice in the past, but in the last few years literature in this area has grown fast, see for example [9–11, 14, 18, 23–25].

2. MODEL EQUATIONS

We first consider the one-dimensional NLSW system of (mass and momentum) equations:

$$\begin{aligned} &\frac{\partial h}{\partial t}+\frac{\partial (uh)}{\partial x}=0\\ &\frac{\partial (uh)}{\partial t}+\frac{\partial}{\partial x}\left(hu^2+\frac{1}{2}gh^2\right)=-gh\frac{\mathrm{d}B}{\mathrm{d}x}-ghS_{\mathrm{f}} \end{aligned} \tag{1}$$

where x is the space coordinate, t the time variable, $h(x,t)$ is the fluid depth, $u(x,t)$ is the horizontal velocity, g is the gravitational constant, $B=B(x)$ is the bed topography function and

$$S_{\mathrm{f}}=n_{\mathrm{m}}^2\frac{u|u|}{h^{4/3}}$$

is the friction slope term, which models bottom friction effects using the Manning empirical form, with n_{m} being the Manning roughness coefficient.

The model can be obtained by depth averaging the Navier–Stokes equations. The water is considered as an incompressible fluid, the pressure is assumed hydrostatic, vertical accelerations negligible and waves are nondispersive. These are reasonable assumptions under the shallow water hypothesis in many practical applications.

System (1) can be written under the form of a conservation law with source terms as a single vector equations:

$$\frac{\partial \mathbf{q}}{\partial t}+\frac{\partial}{\partial x}\mathbf{F}(\mathbf{q})=\mathbf{R}+\mathbf{S} \tag{2}$$

where

$$\mathbf{q}=\begin{bmatrix} h \\ uh \end{bmatrix},\quad \mathbf{F}=\begin{bmatrix} uh \\ hu^2+\frac{1}{2}gh^2 \end{bmatrix},\quad \mathbf{R}=\begin{bmatrix} 0 \\ -gh\dfrac{\mathrm{d}B}{\mathrm{d}x} \end{bmatrix},\quad \mathbf{S}=\begin{bmatrix} 0 \\ -ghS_{\mathrm{f}} \end{bmatrix} \tag{3}$$

The Jacobian matrix of the system is

$$\mathbf{A}(\mathbf{q})=\frac{\partial \mathbf{F}}{\partial \mathbf{q}}=\begin{bmatrix} 0 & 1 \\ c^2-u^2 & 2u \end{bmatrix} \tag{4}$$

with $c=\sqrt{gh}$ being the wave celerity. Then, the eigenvalues of the Jacobian matrix are

$$\lambda_1=u-c,\quad \lambda_2=u+c \tag{5}$$

with the corresponding eigenvectors being

$$\mathbf{r}_1=\begin{bmatrix} 1 \\ u-c \end{bmatrix},\quad \mathbf{r}_2=\begin{bmatrix} 1 \\ u+c \end{bmatrix} \tag{6}$$

If $h>0$, the system is strictly hyperbolic and $\mathbf{A}(\mathbf{q})$ diagonalizes as follows:

$$\mathbf{X}(\mathbf{q})^{-1}\mathbf{A}(\mathbf{q})\mathbf{X}(\mathbf{q})=\mathbf{\Lambda}(\mathbf{q})=\begin{bmatrix} \lambda_1 & 0 \\ 0 & \lambda_2 \end{bmatrix} \tag{7}$$

where $\mathbf{X}(\mathbf{q})$ is a matrix whose columns are the eigenvectors of $\mathbf{A}(\mathbf{q})$, i.e.

$$\mathbf{X}(\mathbf{q})=\begin{bmatrix} 1 & 1 \\ \lambda_1 & \lambda_2 \end{bmatrix} \tag{8}$$

Setting $\lambda^+=\max(0,\lambda)$ and $\lambda^-=\min(0,\lambda)$, we also define the following matrices:

$$\mathbf{\Lambda}(\mathbf{q})^{\pm}=\begin{bmatrix} (\lambda_1)^{\pm} & 0 \\ 0 & (\lambda_2)^{\pm} \end{bmatrix},\quad \mathbf{A}(\mathbf{q})^{\pm}=\mathbf{X}(\mathbf{q})\mathbf{\Lambda}(\mathbf{q})^{\pm}\mathbf{X}(\mathbf{q})^{-1},\quad |\mathbf{A}(\mathbf{q})|=\mathbf{A}(\mathbf{q})^{+}-\mathbf{A}(\mathbf{q})^{-}$$

3. THE NUMERICAL METHOD

Here the well-known approximate Riemann solver of Roe [26] is applied to the NLSW equations. This is a very popular scheme for shallow water flow computations and we will briefly present it here. To discretize the system of equations let, $x_i=i\Delta x$, $x_{i\pm1/2}=(i\pm\frac{1}{2})\Delta x$, where, for simplicity, we assume that Δx is a uniform spatial step. The approximate cell average of the variable $\mathbf{q}$ in the computational cell $I_i = [x_{i-1/2}, x_{i+1/2}]$ at time t is denoted as $\mathbf{Q}_i(t)$, i.e.

$$\mathbf{Q}_i(t) = \frac{1}{\Delta x}\int_{I_i} \mathbf{q}(x,t)\,\mathrm{d}x$$

and the approximate value of $\mathbf{q}$ at $(x_{i+1/2}, t)$ by $\mathbf{q}_{i+1/2}(t)$.

By considering approximations of the solution $\mathbf{q}(x,t)$ that are constant on each finite volume I_i, the value of this approximate solution at the discrete time t^n will be given as $\mathbf{Q}_i^n = [h_i^n, (hu)_i^n]^{\mathrm{T}}$. Next, by denoting $\Delta t^n = t^{n+1} - t^n$, $\mathbf{F}_i^n = \mathbf{F}(\mathbf{Q}_i^n)$ and $\Delta_{i-1/2}(\cdot) = (\cdot)_i - (\cdot)_{i-1}$, we consider the following conservative numerical scheme, assuming initially that $\mathbf{S} = 0$,

$$\mathbf{Q}_i^{n+1} = \mathbf{Q}_i^n - \frac{\Delta t^n}{\Delta x}[\mathbf{F}_{i+1/2}^n - \mathbf{F}_{i-1/2}^n] + \frac{\Delta t^n}{\Delta x}[(\mathbf{R}_{i+1/2}^-)^n + (\mathbf{R}_{i-1/2}^+)^n] \tag{9}$$

Here, the numerical fluxes are defined as

$$\mathbf{F}_{i-1/2}^n = \tfrac{1}{2}(\mathbf{F}_{i-1}^n + \mathbf{F}_i^n) - \tfrac{1}{2}|\mathbf{A}_{i-1/2}^n|\Delta_{i-1/2}\mathbf{Q}^n \tag{10}$$

with

$$\mathbf{A}_{i-1/2}^n = \begin{bmatrix} 0 & 1 \\ (c_{i-1/2}^n)^2 - (u_{i-1/2}^n)^2 & 2u_{i-1/2}^n \end{bmatrix} \tag{11}$$

being the Roe average Jacobian matrix between $\mathbf{Q}_{i-1}^n$ and $\mathbf{Q}_i^n$, with the average velocity and celerity given by

$$u_{i-1/2}^n = \frac{u_{i-1}^n\sqrt{h_{i-1}^n} + u_i^n\sqrt{h_i^n}}{\sqrt{h_{i-1}^n} + \sqrt{h_i^n}}, \quad c_{i-1/2}^n = \sqrt{g\frac{h_i^n + h_{i-1}^n}{2}} \tag{12}$$

The corresponding eigenvalues of $\mathbf{A}_{i-1/2}^n$ are then given by

$$(\lambda_1)_{i-1/2}^n = u_{i-1/2} - c_{i-1/2}, \quad (\lambda_2)_{i-1/2}^n = u_{i-1/2} + c_{i-1/2}$$

and the eigenvectors as

$$(\mathbf{r}_1)_{i-1/2}^n = \begin{bmatrix} 1 \\ (\lambda_1)_{i-1/2}^n \end{bmatrix}, \quad (\mathbf{r}_2)_{i-1/2}^n = \begin{bmatrix} 1 \\ (\lambda_2)_{i-1/2}^n \end{bmatrix}$$

It is well known that the above average values ensure the following property:

$$\Delta_{i-1/2}\mathbf{F} = \mathbf{A}_{i-1/2}\Delta_{i-1/2}\mathbf{Q} = \sum_{p=1}^{2}[\lambda_p\alpha_p\mathbf{r}_p]_{i-1/2} \tag{13}$$

where $\boldsymbol{\alpha}_{i-1/2} = \mathbf{X}_{i-1/2}^{-1}\Delta_{i-1/2}\mathbf{Q}$ are the wave strengths, resulting in

$$(\alpha_{1,2})_{i-1/2} = \frac{\Delta_{i-1/2}(hu) + (-u_{i-1/2} \pm c_{i-1/2})\Delta_{i-1/2}h}{\pm 2c_{i-1/2}}$$

Then, the numerical flux can be expressed in a decomposed form as

$$\mathbf{F}^n_{i-1/2} = \frac{1}{2}(\mathbf{F}^n_{i-1} + \mathbf{F}^n_i) - \frac{1}{2}\sum_{p=1}^{2}[|\lambda_p|\alpha_p \mathbf{r}_p]^n_{i-1/2} \tag{14}$$

In scheme (9) upwinding of the topography source term, see [27, 28], is performed, and by using the matrix identities defined in Section 2, as follows:

$$\mathbf{R}^+_{i-1/2} = (\mathbf{A}^+\mathbf{A}^{-1}\mathbf{R})_{i-1/2} = \tfrac{1}{2}(\mathbf{X}(\mathbf{I} + \mathbf{\Lambda}^{-1}|\mathbf{\Lambda}|)\mathbf{X}^{-1}\mathbf{R})_{i-1/2} \tag{15}$$

and similarly

$$\mathbf{R}^-_{i-1/2} = \tfrac{1}{2}(\mathbf{X}(\mathbf{I} - \mathbf{\Lambda}^{-1}|\mathbf{\Lambda}|)\mathbf{X}^{-1}\mathbf{R})_{i-1/2} \tag{16}$$

Then, using the weights of the decomposition of the source term onto the eigenvectors of the approximate Jacobian, $\boldsymbol{\beta}_{i-1/2} = \mathbf{X}^{-1}_{i-1/2}\mathbf{R}_{i-1/2}$, and when the following discretization of the numerical source term is used

$$\mathbf{R}_{i-1/2} = \begin{bmatrix} 0 \\ (-c_{i-1/2})^2(B(x_i) - B(x_{i-1})) \end{bmatrix} \tag{17}$$

the following equality holds:

$$\Delta_{i-1/2}\mathbf{F} - \mathbf{R}_{i-1/2} = 0 \tag{18}$$

and we obtain

$$\mathbf{R}^+_{i-1/2} = \frac{1}{2}\sum_{p=1}^{2}[\beta_p \mathbf{r}_p(1 + \mathrm{sgn}(\lambda_p))]_{i-1/2} \tag{19}$$

$$\mathbf{R}^-_{i+1/2} = \frac{1}{2}\sum_{p=1}^{2}[\beta_p \mathbf{r}_p(1 - \mathrm{sgn}(\lambda_p))]_{i+1/2} \tag{20}$$

with

$$(\beta_{1,2})_{i-1/2} = \pm\frac{c_{i-1/2}\Delta_{i-1/2}B}{2}$$

The numerical scheme presented above allows nonphysical numerical solutions (expansion shocks), [29]. These can be avoided by applying Harten's [30] entropy correction (essentially a modification to the moduli of λ), which ensures that the approximate solution satisfies an entropy condition, see for example [29, 31] for applications.

Conserving the stability requirements, each time step Δt^n is calculated based on the following Courant–Friedrichs–Lewy (CFL) condition:

$$\Delta t^n = \frac{\Delta x Cr}{\max_i\{\max_p |\lambda|\}} \tag{21}$$

where Cr is the Courant number between zero and one.

When the friction term, which does not involve spatial derivatives, is assumed present ($\mathbf{S} \neq 0$), it can be discretized in a semi-implicit way to avoid numerical oscillations, as proposed in [32]. The final expression of the numerical scheme then becomes

$$\mathbf{Q}_i^{n+1} = \frac{\mathbf{Q}_i^n - \dfrac{\Delta t^n}{\Delta x}[\mathbf{F}_{i+1/2}^n - \mathbf{F}_{i-1/2}^n + (\mathbf{R}_{i+1/2}^-)^n + (\mathbf{R}_{i-1/2}^+)^n] + \Delta t^n \theta \mathbf{S}_i^n}{1 - (1-\theta)\Delta t^n \mathbf{S}_i^n / \mathbf{Q}_i^n} \tag{22}$$

in which θ is a weight of the implicitness of the friction term. We note here that sometimes modellers omit the inclusion of the friction term from their calculations.

4. CONSERVATION PROPERTY AND THE WET/DRY TREATMENT

An important property of system (1) is related to the topography source term: the shallow water system admits nontrivial steady states. They are characterized by

$$\begin{aligned} \frac{\partial(uh)}{\partial x} &= 0 \\ \frac{\partial}{\partial x}\left(hu^2 + \frac{1}{2}gh^2\right) &= -gh\frac{\mathrm{d}B}{\mathrm{d}x} \end{aligned} \tag{23}$$

i.e.

$$\begin{aligned} (uh) &= \text{constant} \\ u^2h + g(h+B) &= \text{constant} \end{aligned} \tag{24}$$

A particular case that provides a benchmark for many numerical schemes is the still water steady state (flow at rest), i.e. when $u = 0$ and $h + B = \text{constant}$. In [27] the concept of a well-balanced condition, called the C-Property or conservation property, was introduced. A given scheme would satisfy the C-Property if, in the case of a flow at rest, there is an exact balance between the discrete components of the flux and a given source term approximating this stationary solution. Thus, when numerically treating the source terms, for the C-Property to be satisfied exactly or approximately (to order $O(\Delta x^2)$) one must ensure that this equilibrium solution would not be perturbed. The numerical scheme presented in the last section is well balanced in this sense.

In [33] an extension of the C-Property was introduced in order to take into account wet/dry fronts. According to this extension, a numerical scheme is considered to be well balanced if it can solve exactly steady-state solutions corresponding to flow at rest regardless of including wet/dry transitions or not. If no modifications are made, the numerical scheme presented in the previous section is not well balanced in this sense. In previous works [32, 34], a two-dimensional model was presented for unsteady flow simulations based on a first-order explicit upwind finite volume scheme on unstructured meshes where the wetting/drying problem was included from a still water steady-state approach with the requirement of exact mass conservation at the discrete level. A redefinition of the numerical source term was proposed in [32, 34] that allows to override the above problem in the discrete representation of wet/dry fronts over adverse steep slopes.

If we consider the interface $x_{i+1/2}$ placed between a wet cell I_i and a dry cell I_{i+1}, we now define

$$\mathbf{R}_{i+1/2}=\begin{cases}\begin{bmatrix}0\\-(c^n_{i+1/2})^2h^n_i\end{bmatrix} & \text{if } h^n_i<B(x_{i+1})-B(x_i)\\[2ex] \begin{bmatrix}0\\(c^n_{i+1/2})^2h^n_{i+1}\end{bmatrix} & \text{if } h^n_{i+1}<B(x_i)-B(x_{i+1})\\[2ex] \begin{bmatrix}0\\-(c^n_{i+1/2})^2(B(x_{i+1})-B(x_i))\end{bmatrix} & \text{in other cases}\end{cases}\qquad(25)$$

This modification of the numerical source term is a redefinition of the discretized topography function (essentially a local redefinition of the bottom level gradient at the wet/dry interface) and is justified by the assumption of a piecewise constant bottom representation in each cell. When the topography emerges at an interface it is redefined in the dry cell in order to avoid the appearance of spurious pressure forces and to satisfy condition (18). This treatment does not diffuse the front and no spurious oscillations appear in the free surface. In terms of the numerical scheme, the values of $\boldsymbol{\beta}$ in (19) and (20) are redefined accordingly.

While with this modification of the discretized topography function one can treat situations of emerging topography for a flow at rest, further modifications have to be made for a flow in motion ($u\neq 0$) because otherwise the water could overtop steps of arbitrary size. This is important in the cases considered in the present work that involve the runup of waves on complex topographies. In [34] these situations were treated by imposing the following condition at the wet cell I_i:

$$(uh)^n_i=0\qquad(26)$$

in order to simulate the fact that the water mass flow across a wet/dry front is zero. However, with this treatment the computed velocities of an advancing wet/dry front are not correctly simulated. A new improvement was proposed in [33] based on the remark that (26) is only natural at the wet/dry front and not in the whole wet cell and therefore it has to be treated like an internal boundary. By considering the situation where the bottom topography emerges at the interface $x_{i+1/2}$ at time t^n and I_{i+1} is a dry cell (i.e. $\mathbf{Q}^n_{i+1}=[0,0]^{\mathrm{T}}$), the following procedure was proposed:

- The modified numerical source term given by (25) is computed.
- A new state $\widetilde{\mathbf{Q}}^n_i$ defined by

$$\widetilde{\mathbf{Q}}^n_i=\begin{bmatrix}h^n_i\\0\end{bmatrix}\qquad(27)$$

  is considered.
- $\mathbf{Q}^{n+1}_i$ and $\mathbf{Q}^{n+1}_{i+1}$ are computed using scheme (22) with the numerical fluxes $\mathbf{F}^n_{i+1/2}$ and source term $\mathbf{R}^{\pm}_{i+1/2}$ associated with the states $\widetilde{\mathbf{Q}}^n_i$, $\mathbf{Q}^n_{i+1}$ and the modified source term (25).

The numerical treatment is similar if I_{i+1} is the wet cell and I_i is the dry one. As it was pointed out in [33, 35], this numerical treatment avoids the appearance of negative values of h at the dry cell and that the smaller the momentum absolute value is at the wet cell, the better this approximation would be.

5. HIGH-RESOLUTION SCHEME

The numerical scheme presented in Section 3 is a standard first-order upwind type scheme. Usually though, accuracy of higher than first order is required for practical calculations. The accuracy of the scheme can be improved, without introducing spurious oscillations into the solution, by the application of flux-limiting techniques. These ensure second-order accuracy in smooth regions of the flow, while enforcing a total variation diminishing (TVD) property, see for example [14, 30, 31, 36]. This can be achieved by including a higher-order correction term in the numerical flux as

$$\mathbf{F}^{\mathrm{TVD}}_{i-1/2} = \mathbf{F}^{\mathrm{FO}}_{i-1/2} + \Phi^n_{i-1/2}(\mathbf{F}^{\mathrm{HO}}_{i-1/2} - \mathbf{F}^{\mathrm{FO}}_{i-1/2}) \tag{28}$$

where Φ is a nonlinear flux-limiter function. Then if we use the Lax–Wendroff numerical flux as a higher-order flux and the Roe numerical flux as a first-order one, we get

$$\mathbf{F}^{\mathrm{HO}}_{i-1/2} - \mathbf{F}^{\mathrm{FO}}_{i-1/2} = \frac{1}{2}\left(\mathbf{X}|\mathbf{\Lambda}|\left(\mathbf{I} - \frac{\Delta t^n}{\Delta x}|\mathbf{\Lambda}|\right)\mathbf{X}^{-1}\right)^n_{i-1/2}\Delta_{i-1/2}\mathbf{Q}^n$$

Then by using (28) the TVD numerical flux becomes

$$\mathbf{F}^n_{i-1/2} = \tfrac{1}{2}(\mathbf{F}^n_i + \mathbf{F}^n_{i-1}) - \tfrac{1}{2}(\mathbf{X}|\mathbf{\Lambda}|\mathbf{L}\mathbf{X}^{-1})^n_{i-1/2}\Delta_{i-1/2}\mathbf{Q}^n \tag{29}$$

in which

$$\mathbf{L} = \mathrm{diag}\left(1 - \Phi(\theta_p)\left(1 - \frac{\Delta t^n}{\Delta x}|\lambda_p|\right)\right)$$

where

$$\theta_p = \frac{(\alpha_p)_{s-1/2}}{(\alpha_p)_{i-1/2}}, \quad s = \begin{cases} i-1 & \text{if } \lambda_p > 0 \\ i+1 & \text{if } \lambda_p < 0 \end{cases}$$

The decomposed form of (29) is then given as

$$\mathbf{F}^n_{i-1/2} = \frac{1}{2}(\mathbf{F}^n_i + \mathbf{F}^n_{i-1}) - \frac{1}{2}\sum_{p=1}^{2}[\alpha_p|\lambda_p|(1 - \Phi(\theta_p)(1 - |v_p|))\mathbf{r}_p]^n_{i-1/2} \quad \text{with } v_p = \frac{\Delta t^n}{\Delta x}\lambda_p$$

Next, if a balance is to be maintained between the numerical flux and source terms, a corresponding higher-order correction must also be applied to the source term approximation following [36]. The flux-limited numerical source, which maintains the balance achieved by the first-order discretization (and also satisfies the C-Property), takes the form

$$\mathbf{R}^{\pm}_{i-1/2} = \tfrac{1}{2}[\mathbf{X}(\mathbf{I} \pm \mathbf{\Lambda}^{-1}|\mathbf{\Lambda}|\mathbf{L})\mathbf{X}^{-1}\mathbf{R}]_{i-1/2} \tag{30}$$

or in decomposed form

$$\mathbf{R}^{\pm}_{i-1/2} = \frac{1}{2}\sum_{p=1}^{2}[\beta_p\mathbf{r}_p(1 \pm \mathtt{sgn}(\lambda_p)(1 - \Phi(\theta_p)(1 - |v_p|)))]_{i-1/2} \tag{31}$$

A number of different flux limiters can be used, including Minmod, Van Leer, Van Albada, Monotonized Central and Superbee, see for example [29, 37].

We note here that one of the objectives of the present work is to apply the corrections presented in Section 4 on the second-order scheme and access its performance and later extend it in two dimensions.

6. NUMERICAL TESTS AND RESULTS IN ONE DIMENSION

The extended numerical model is now well adapted to simulate steady states as, for example, the flow can be far from a solitary wave, and cases of emerging topographies of arbitrary profile for the case of runup and rundown of long waves. In all practical implementations, a threshold of 5×10^{-14} has been used in order to identify a dry cell.

6.1. Tsunami runup on a plane beach

As part of the Third International Workshop on Long-Wave Runup Models in 2004 [38], several benchmark problems were specified to allow the comparison of numerical, analytical and experimental data. The web site of the conference is http://www.cee.cornell.edu/longwave, where all the relevant data are provided.

The first benchmark problem has a uniform, frictionless, steep sloping beach with $B(x,t)=-x$, and initially motionless water with the shoreline positioned at $x=0$. An incoming wave is induced by a nonzero initial surface elevation, specified by data provided for $x\in[0,50\,000]$ in increments of 50 m. Data for the analytical solution of the surface elevation and velocity, at three separate times $t=160$, 175, and 220 s, were provided. The initial value problem technique introduced by Carrier *et al.* [5] was used to produce the benchmark data. The position and velocity of the shoreline were also provided for $t\in[0,350]$ s. Wave breaking is not included in this problem. The shape of the initial free surface is shown in Figure 1 (this shape is akin to slide-generated tsunami, but with zero initial velocity).

We computed this problem over a domain $x\in[-500,50\,000]$ m with a uniform partition and we present the results for the water surface elevation and velocity using $\Delta x=20$ m and $\mathrm{CFL}=0.5$. In Figures 2–4, we compare the results in terms of the surface elevation and velocity for the first- and second-order scheme (using the Minmod limiter) at the three given times. In the figures, only small portions of the computational domain near the beach are shown (in order to be able to distinguish differences in the results). The results for the second-order scheme are clearly better than the first-order one and agree very well with the analytical solution, only in the case of $t=220$ s the numerical solution slightly overpredicts the shoreline position. Convergence to the analytical solution was observed as the grid was refined.

In order to capture the fine-scale motion of the shoreline, which occurred over a small fraction of the entire domain, computational grid cells were clustered near the shoreline. In Figure 5 the motion of the computed shoreline is compared with the exact solution using 1000 grid points clustered in the area $[-250,250]$. The computed shoreline movement follows closely the provided exact solution, showing the initial rundown and subsequent runup on the plane beach, but the computed velocity profile slightly over and under predicts the provided exact solution, especially at relatively larger velocity values, similar comments were made in [35]. Nevertheless, the computed solution follows the overall exact velocity profile.

DOI: 10.1002/fld

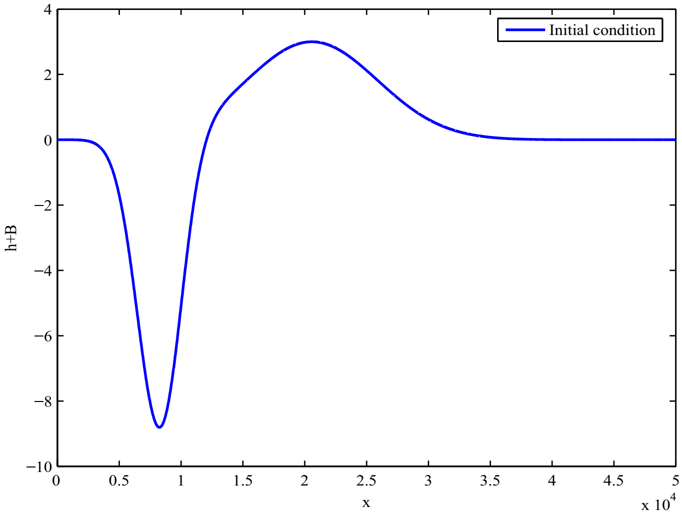

Figure 1. Initial free surface elevation for tsunami runup.

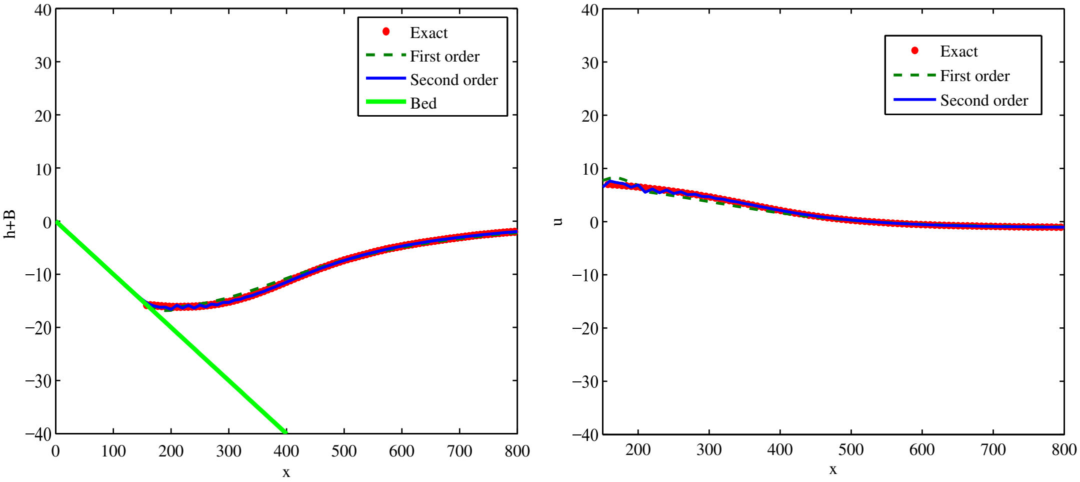

Figure 2. Tsunami runup on a plane beach at $t=160\,\mathrm{s}$: surface elevation (left) and velocity (right).

6.2. Runup of solitary waves on a plane beach

This problem is presented here as to compare numerical and experimental results of the runup, rundown and wave breaking of a solitary wave on a plane beach. Synolakis [3] presented a series of surface profiles from his runup experiments for a beach of slope of 1:19.85, that is

$$B(x)=\begin{cases}-x\tan\beta & x\leqslant\cot\beta\\ -1 & x>\cot\beta\end{cases}$$

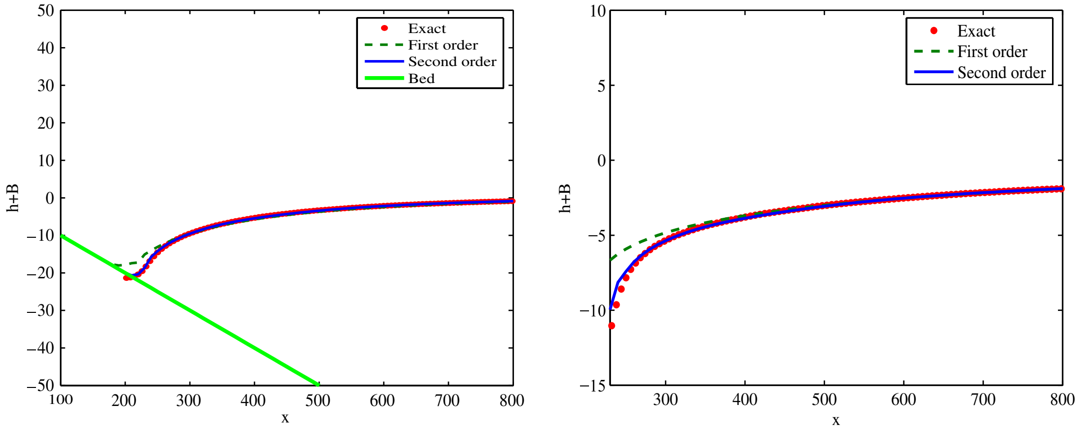

Figure 3. Tsunami runup on a plane beach at $t=175$ s: surface elevation (left) and velocity (right).

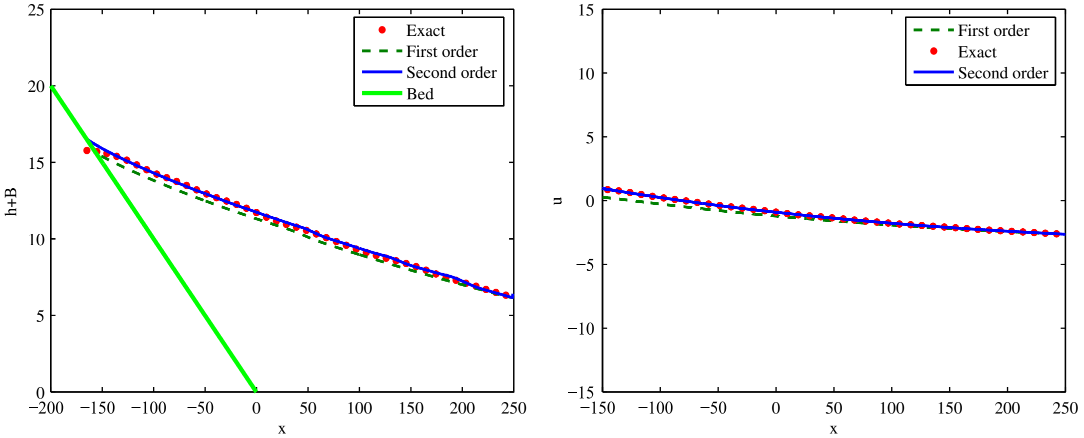

Figure 4. Tsunami runup on a plane beach at $t=220$ s: surface elevation (left) and velocity (right).

with $\tan\beta \approx 0.0504$. Although it is well known that solitary waves are not classical solutions of the NLSW equations, it has been found that, for small amplitudes and over limited distances, Synolakis's solution provides a good model for beach inundation, and his sets of data have been extensively used in order to validate numerical models. Figure 6 shows a schematic of the experiments with H indicating the incident wave height, β the beach angle and d the depth of stagnant water. An initial solitary wave is positioned at point X_1 that is located at half the wave length from the toe of the beach located at X_0. A Mianning coefficient $n_{\mathrm{m}}=0.01$ was used in order to define the glass surface roughness used in the experiments and we considered a computational domain for $x \in [-10, 100]$ m.

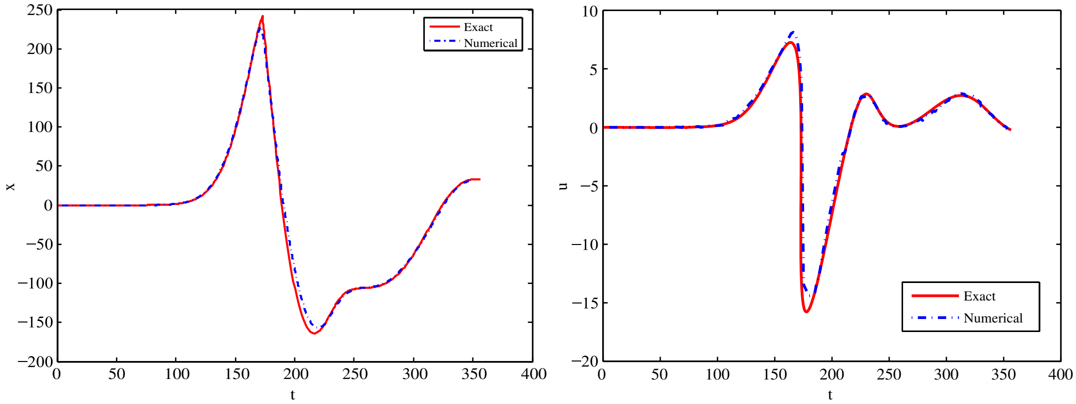

Figure 5. Tsunami runup on a plane beach: position of the shoreline (left) and shoreline velocity (right) as functions of time.

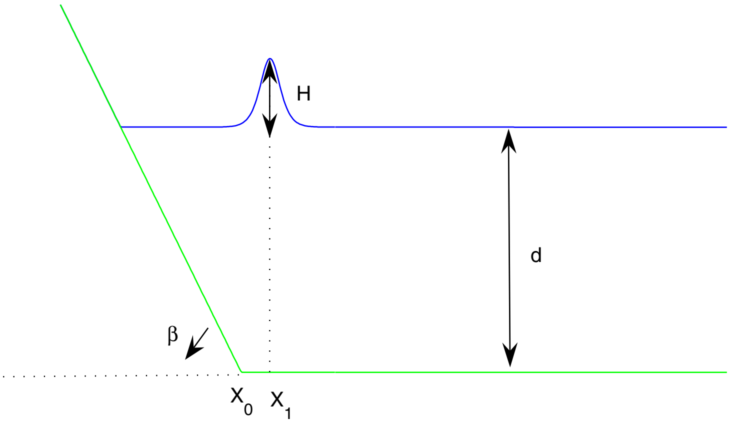

Figure 6. Definition figure of solitary wave runup on a plane beach.

At $t=0$ the incident wave is described by

$$\eta(x,0)=\frac{H}{d}\operatorname{sech}^2(\gamma(x-X_1))$$

where $\gamma=\sqrt{3H/4d}$ with initial velocity

$$u(x,0)=-\sqrt{g/d}\,\eta(x,0)$$

and

$$X_1=\sqrt{\frac{4d}{3H}}\operatorname{arcosh}\left(\sqrt{\frac{1}{0.05}}\right)$$

The left boundary condition is transmissive and is kept sufficiently far from the toe of the beach in order to prevent any interaction with the water waves during the runup process.

Two different cases are presented for comparison with the numerical model. For the first case, the incident wave height is $H/d = 0.04$ and for the second one $H/d = 0.28$ (a larger amplitude solitary wave). According to Synolakis [3] wave breaking occurred during rundown when $H/d > 0.044$ and hence breaking did not occur for the $H/d = 0.04$ wave (although it very nearly broke on the rundown). The $H/d = 0.28$ wave broke strongly during both the runup and rundown phases of the motion. The CFL value used for this problem was 0.5, with $\Delta x = 0.1$, $\theta = 0.5$ in (22) and the Minmod limiter was used.

Figure 7 presents the series of the free surface profiles when $H/d = 0.04$ for different nondimensional times. Figure 7 presents both the runup and rundown processes. At times $t\sqrt{g/h} = 20, 26, 32$ the incident wave approaches the shoreline and by time $t\sqrt{g/h} = 38$ has started its runup on the beach and the numerical solution follows very closely the experimental results. Notice that the shoreline elevation and the runup tongue thickness are predicted well by the numerical scheme. The maximum runup, R/d, measured in [3] for this problem was $R/d = 0.156$. The numerical scheme predicted that value, but we note here that this is a value that strongly depends on the value of the friction coefficient. The rundown of the wave is also well predicted by the finite volume scheme. The experimental observation that the wave nearly broke down during rundown can be seen at $t\sqrt{g/h} = 62$ where the numerical results look similar to that of a hydraulic jump.

Figure 8 presents the series of surface profiles with $H/d = 0.28$. At times $t\sqrt{g/h} = 10, 15, 20$, as the wave shoals, the computed front face has become steeper earlier than the experimental wave due to the large wave height and the limitation of the NLSW equations that do not include higher-order dispersive terms to balance the nonlinear effects. The experimental wave breaks around $t\sqrt{g/h} = 20$ and the computed solution represents this as a bore and stores the water spilled from the breaking wave behind the front face. The vertical front indicates an abrupt change of the flow velocity from the bore to the undisturbed water ahead. Then the bore collapses as breaking occurs. Because of volume conservation, the computed solution fully recovers when breaking stops and a good agreement is maintained between the numerical and experimental results, until the water reaches the highest point around $t\sqrt{g/h} = 45$. In [3] an interval of the maximum runup value for a breaking wave was given, that is $R/d \in [0.918(H/d)^{0.606}, 1.109(H/d)^{0.582}] \approx [0.42, 0.53]$ and the value predicted by the numerical scheme is well within this interval. Then the water is receding creating a breaking wave near the still water line. This is created as the retreating flow interacts with the wave tail and creates a region of large free surface curvature near the initial shoreline position. In the numerical solution this is approximated as a hydraulic jump conserving the flow volume behind it. Small discrepancies in the runup tongue, which is thinner than the experimental data, begin to show at time $t\sqrt{g/h} = 55$. However, both the position of the jump and the height difference across the jump are predicted well by the numerical scheme. The qualitative agreement between the experimental and numerical results resumes when breaking stops at the end of the rundown process, demonstrating the resilience of the scheme. We emphasize that convergence towards a steady state of a flow at rest is accurately computed, after the total reflection of the incident wave, whereas other schemes used in the literature may be unable to provide correct results related to this convergence since nonphysical oscillations are generated. Due to this reason, authors sometimes do not present results for large values of time, for the following rundown that is more difficult to compute, and only present their results for the runup process.

In Figure 9 the time history of the relative volume conservation error is presented. The result shows no volume change until the wave breaks and propagates over the slope. The error shows

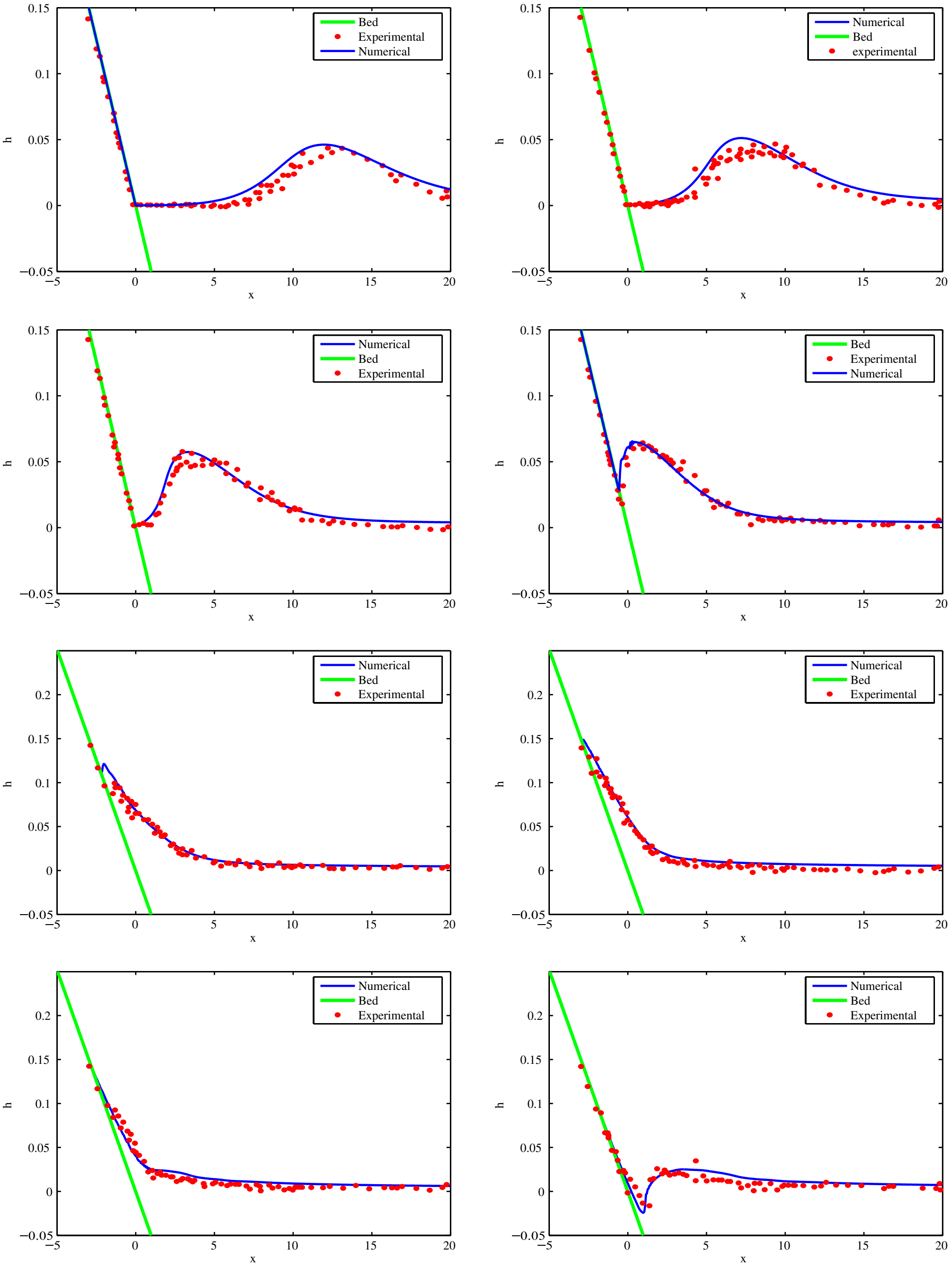

Figure 7. Surface elevation of solitary wave runup on a plane beach for $H/d = 0.04$ at times $t\sqrt{g/h} = 20, 26, 32, 38, 44, 50, 56, 62$ (from upper left).

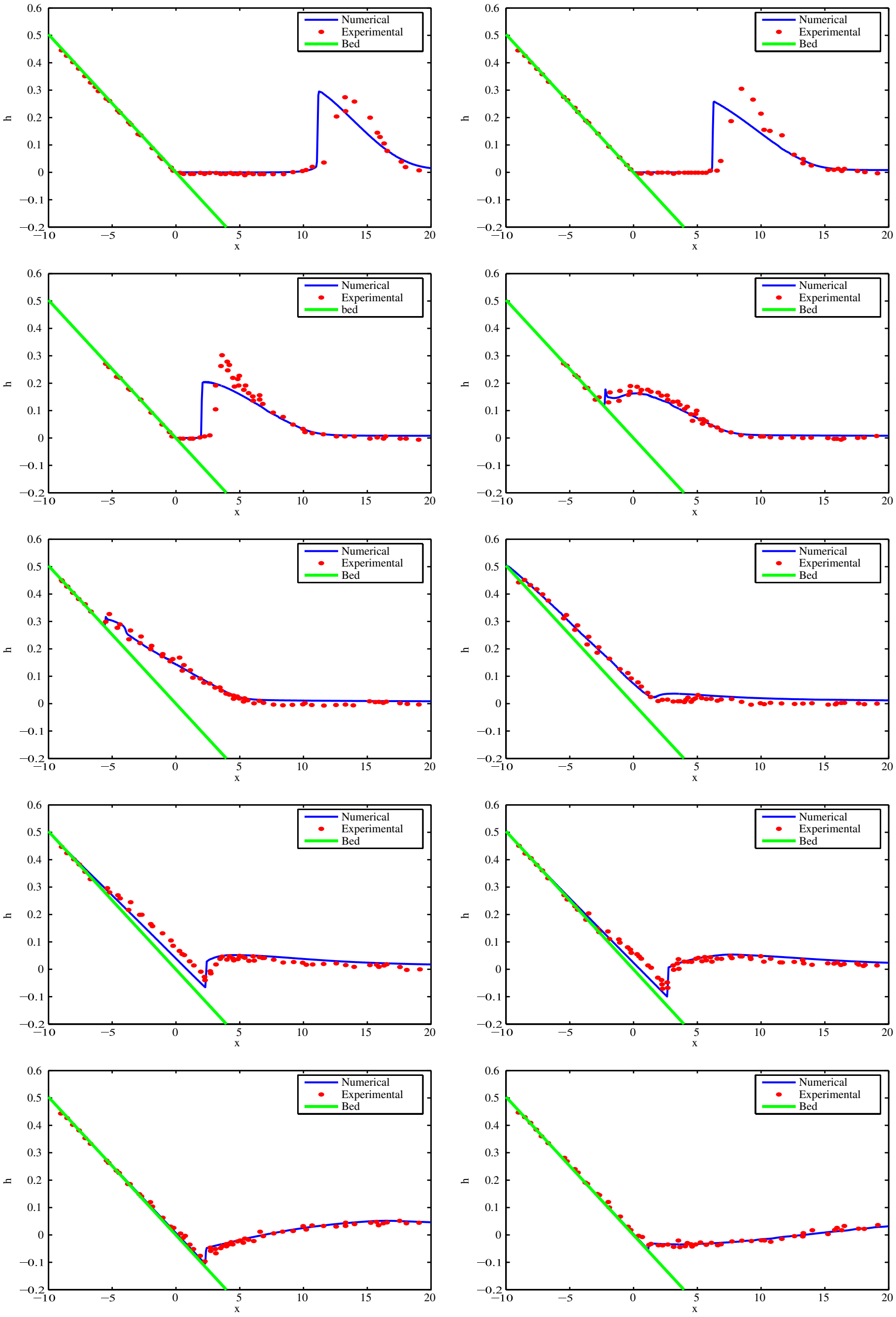

Figure 8. Surface elevation of solitary wave runup on a plane beach for $H/d = 0.28$ at times $t\sqrt{g/h} = 10$, 15, 20, 25, 30, 45, 55, 60, 70, 80 (from upper left).

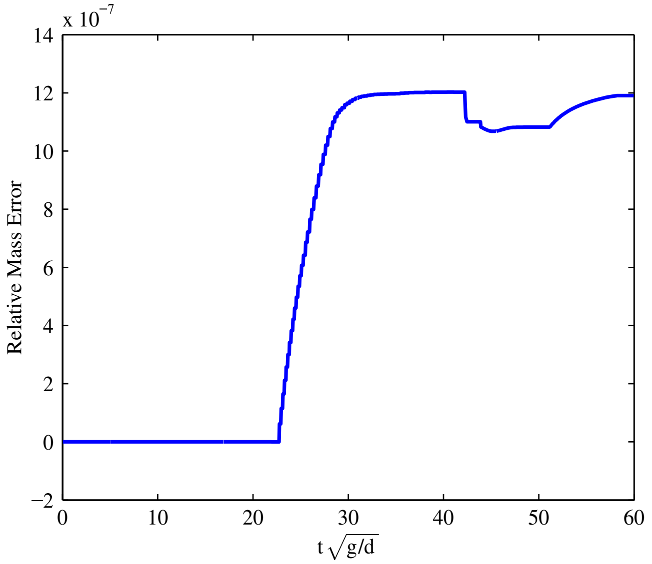

Figure 9. Relative mass volume conservation error for solitary wave runup on a plane beach with $H/d = 0.28$.

small increase when the bore hits the still water line and then becomes stable up to the point the water reaches the highest point. Then at the beginning of the rundown a small decrease is observed up to the point of the hydraulic jump development. The maximum error is $12 \times 10^{-7}\%$ of the initial solitary wave volume. All the results presented here compare well or in favour with the results presented, for example, in [6, 9, 20] among others.

6.3. Tsunami generation and runup due to a two-dimensional landslide

This benchmark problem is from [4] and was also used as a benchmark problem in the Third International Workshop on Long-Wave Runup Models where all relevant data were also provided. Here, the modellers were asked to predict the free surface elevation and runup associated with a translating Gaussian-shaped mass, initially at the shoreline. In dimensional form, the seabed can be described by

$$B(x,t) = B_0(x) + h_0(x,t)$$

where $B_0(x) = -x \tan\beta$ is the beach slope, and

$$h_0(x,t) = \delta \exp\left[-\left(2\sqrt{\frac{x\mu^2}{\delta\tan\beta}} - \sqrt{\frac{g}{\delta}}\mu t\right)^2\right]$$

is the time-dependant perturbation of the seabed, in which δ is the maximum vertical slide thickness, μ is the thickness/slide length and β is the beach slope. Once in motion, the mass moves at constant acceleration.

DOI: 10.1002/fld

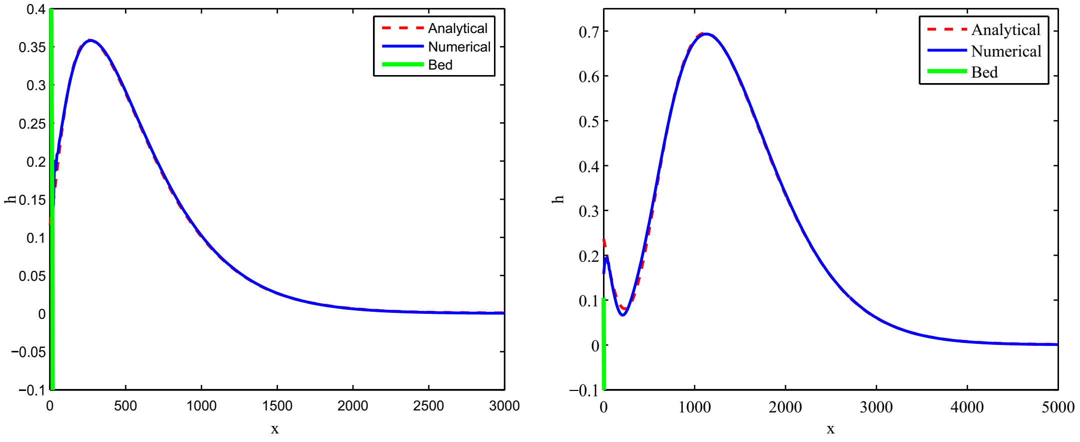

Figure 10. Tsunami generation and runup: surface elevation for Case A at times $t' = 0.5, 1.5$.

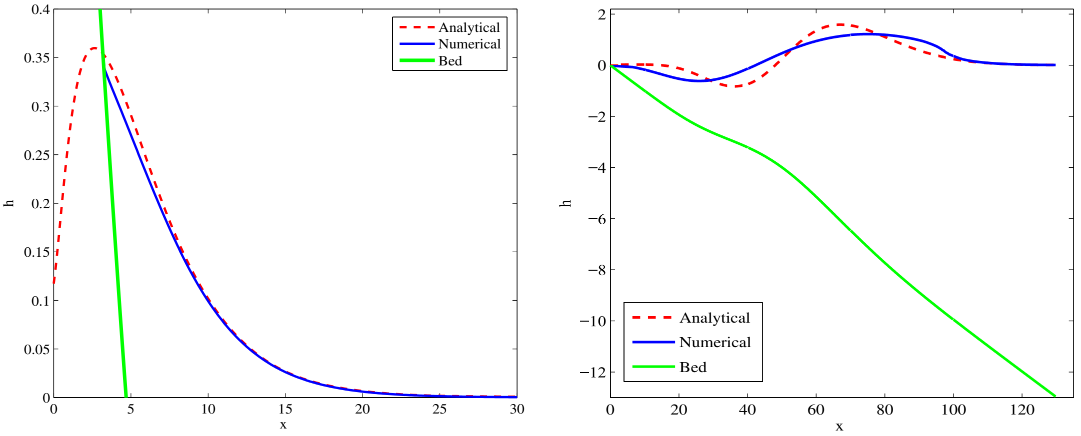

Figure 11. Tsunami generation and runup: surface elevation for Case B at times $t' = 0.5, 4.5$.

We compute the results for two cases:

- Case A: $\tan\beta/\mu = 10$ where $\mu = 0.01$ (very thin mass layer), $\beta = 5.7°$ and $\delta = 1$ m.
- Case B: $\tan\beta/\mu = 1$ with $\mu = 0.1$, $\beta = 5.7°$ and $\delta = 1$ m.

The computational domain is for $x \in [0, 5000]$ m, with $\Delta x = 2$ m used, for Case A, while $x \in [0, 130]$ and $\Delta x = 0.1$ for Case B. The CFL value used for this problem was 0.8 using the Minmod limiter.

We compare the computed solutions for the surface elevation with the data from the analytical solutions obtained for the linear shallow water equation equations from [4] at the nondimensional times: $t' = \sqrt{g/\delta}\mu t = 0.5, 1.5$ for the first case and at times $t' = 0.5, 4.5$ for the second one.

In Figure 10 and for Case A, agreement with the analytical solutions is very good on predicting the wave runup and wave propagation on thin slide. For this case the offshore wave and height and shape agree very well with the analytical solution with small differences near the shoreline.

Agreement for Case B, using any model other than the linear shallow water wave equations, is expected to be poor. As it can be seen in Figure 11, at an early time the numerical result and the analytical solution are close (since the accumulating effects of nonlinearity are small relative to the linear driving force). For a later time this is no longer the case since nonlinear propagation effects become important. In this case, omission of the nonlinear terms, in deriving the analytical solution, leads to difference in the solutions, which become stronger in time and the analytical solution is not adequate for this case. Similar observations and results were made by the workshop participants.

7. TWO-DIMENSIONAL EXTENSION

In this section we present the two-dimensional NLSW equations along with an extension of the numerical scheme and of the wet/dry treatment.

In two dimensions the NLSW equations are given as

$$\frac{\partial \mathbf{q}}{\partial t} + \frac{\partial}{\partial x}\mathbf{F}(\mathbf{q}) + \frac{\partial}{\partial y}\mathbf{G}(\mathbf{q}) = \mathbf{R}(\mathbf{q}, x, y) + \mathbf{S}(\mathbf{q}, x, y) \tag{32}$$

where now

$$\mathbf{q} = \begin{bmatrix} h \\ hu \\ hv \end{bmatrix}, \quad \mathbf{F}(\mathbf{q}) = \begin{bmatrix} hu \\ hu^2 + \frac{1}{2}gh^2 \\ huv \end{bmatrix}, \quad \mathbf{G}(\mathbf{q}) = \begin{bmatrix} hv \\ huv \\ hv^2 + \frac{1}{2}gh^2 \end{bmatrix}$$

with $[u, v]^{\mathrm{T}}$ being the vector velocity field. The geometrical source term is given as $\mathbf{R} = \mathbf{R}_1 + \mathbf{R}_2$ in which

$$\mathbf{R}_1 = \begin{bmatrix} 0 \\ -gh\frac{\partial}{\partial x}B(x, y) \\ 0 \end{bmatrix}, \quad \mathbf{R}_2 = \begin{bmatrix} 0 \\ 0 \\ -gh\frac{\partial}{\partial y}B(x, y) \end{bmatrix}$$

and the friction source vector given as

$$\mathbf{S} = \begin{bmatrix} 0 \\ -ghS_f^x \\ -ghS_f^y \end{bmatrix}$$

with

$$S_f^x = n_m^2 u\sqrt{u^2 + v^2}h^{-4/3} \quad \text{and} \quad S_f^y = n_m^2 v\sqrt{u^2 + v^2}h^{-4/3}$$

The Jacobian matrices of system (32) are now

$$\frac{\partial \mathbf{F}}{\partial \mathbf{q}} = \mathbf{A} = \begin{bmatrix} 0 & 1 & 0 \\ c^2 - u^2 & 2u & 0 \\ -uv & v & u \end{bmatrix}, \quad \frac{\partial \mathbf{G}}{\partial \mathbf{q}} = \mathbf{B} = \begin{bmatrix} 0 & 0 & 1 \\ -uv & v & u \\ c^2 - v^2 & 0 & 2v \end{bmatrix}$$

The eigenvalues of **A** and **B** are

$$\lambda_1^F = u - c, \quad \lambda_2^F = u, \quad \lambda_3^F = u + c \tag{33}$$

and

$$\lambda_1^G = v - c, \quad \lambda_2^G = v, \quad \lambda_3^G = v + c \tag{34}$$

with corresponding eigenvectors

$$\mathbf{r}_1^F = \begin{bmatrix} 1 \\ u - c \\ v \end{bmatrix}, \quad \mathbf{r}_2^F = \begin{bmatrix} 0 \\ 0 \\ c \end{bmatrix}, \quad \mathbf{r}_3^F = \begin{bmatrix} 1 \\ u + c \\ v \end{bmatrix} \tag{35}$$

$$\mathbf{r}_1^G = \begin{bmatrix} 1 \\ u \\ v - c \end{bmatrix}, \quad \mathbf{r}_2^G = \begin{bmatrix} 0 \\ -c \\ 0 \end{bmatrix}, \quad \mathbf{r}_3^G = \begin{bmatrix} 1 \\ u \\ v + c \end{bmatrix} \tag{36}$$

The finite volume formulation imposes conservation laws in a control volume which reduces to a two-dimensional cell for depth integrated problems. Integrating system (32) over a cell Ω_i and applying the Gauss divergence theorem to the flux integral, one obtains

$$\frac{\partial}{\partial t} \int_{\Omega_i} \mathbf{q} \, \mathrm{d}\Omega + \int_{\Gamma_i} (\mathbf{F} n_x + \mathbf{G} n_y) \, \mathrm{d}\Gamma = \int_{\Omega_i} (\mathbf{R} + \mathbf{S}) \, \mathrm{d}\Omega \tag{37}$$

where Γ_i is the cell boundary and $[n_x, n_y]^{\mathrm{T}}$ the outward normal vector. Then by denoting $|\Omega_i|$ the cell area and by **Q** the average value of the conserved quantities over the volume at a given time, from Equation (37) the following conservation equation can be written for every cell

$$\frac{\mathrm{d}\mathbf{Q}}{\mathrm{d}t} = -\frac{1}{|\Omega_i|} \int_{\Gamma_i} (\mathbf{F} n_x + \mathbf{G} n_y) \, \mathrm{d}\Gamma + \widetilde{\mathbf{R}} + \widetilde{\mathbf{S}} \tag{38}$$

in which $\widetilde{\mathbf{R}}$ and $\widetilde{\mathbf{S}}$ are average quantities stored at the center of the cell. In this work we used uniform rectangular cells with dimensions $(\Delta x, \Delta y)$ in a Cartesian grid and integrating equation (38) with a time step Δt^n we obtain

$$\mathbf{Q}_{ij}^{n+1} = \mathbf{Q}_{ij}^n - \frac{\Delta t^n}{\Delta x} [\mathbf{F}_{i+1/2,j}^n - \mathbf{F}_{i-1/2,j}^n] - \frac{\Delta t^n}{\Delta y} [\mathbf{G}_{i,j+1/2}^n - \mathbf{G}_{i,j-1/2}^n] + \Delta t^n (\mathbf{R}_{i,j}^n + \mathbf{S}_{i,j}^n) \tag{39}$$

where now (i, j) indicates the cell centroid, the half indices $(i \pm \frac{1}{2})$ an $(j \pm \frac{1}{2})$ indicate the cell interfaces and $\mathbf{F}_{i\pm 1/2,j}$ and $\mathbf{G}_{i,j\pm 1/2}$ are the numerical fluxes, with $\mathbf{R}_{i,j}$ and $\mathbf{S}_{i,j}$ being the source term vectors.

Solving locally linearized Riemann problems, at each cell interface, based on the Roe solver, the average values for the velocities and water depth are obtained as

$$u_{i\pm 1/2,j}=\frac{\sqrt{h_{i\pm 1,j}}u_{i\pm 1,j}+\sqrt{h_{ij}}u_{ij}}{\sqrt{h_{i\pm 1,j}}+\sqrt{h_{ij}}},\quad v_{i,j\pm 1/2}=\frac{\sqrt{h_{i,j\pm 1}}v_{i,j\pm 1}+\sqrt{h_{ij}}v_{ij}}{\sqrt{h_{i,j\pm 1}}+\sqrt{h_{ij}}} \tag{40}$$

and

$$h_{i\pm 1/2,j}=\tfrac{1}{2}(h_{i\pm 1,j}+h_{ij}),\quad h_{i,j\pm 1/2}=\tfrac{1}{2}(h_{i,j\pm 1}+h_{ij}) \tag{41}$$

Then, the Roe-averaged eigenvalues and eigenvectors in two dimensions can be calculated.

This leads to numerical fluxes expressed for the second-order flux-limiting scheme as [36]

$$\mathbf{F}^n_{i+1/2,j}=\frac{1}{2}(\mathbf{F}^n_{i+1,j}+\mathbf{F}^n_{ij})-\frac{1}{2}\sum_{p=1}^{3}[\alpha^F_p|\lambda^F_p|(1-\Phi(\theta^F_p)(1-|v^F_p|))\mathbf{r}^F_p]^n_{i+1/2,j} \tag{42}$$

$$\mathbf{G}^n_{i,j+1/2}=\frac{1}{2}(\mathbf{G}^n_{i,j+1}+\mathbf{G}^n_{ij})-\frac{1}{2}\sum_{p=1}^{3}[\alpha^G_p|\lambda^G_p|(1-\Phi(\theta^G_p)(1-|v^G_p|))\mathbf{r}^G_p]^n_{i,j+1/2} \tag{43}$$

in which the wave strengths are now

$$(\alpha^F_{1,3})_{i+1/2,j}=\frac{\Delta_{i+1/2,j}(hu)+(-u_{i+1/2,j}\pm c_{i+1/2,j})\Delta_{i+1/2,j}h}{\pm 2c_{i+1/2,j}}$$

$$(\alpha^F_2)_{i+1/2,j}=\frac{\Delta_{i+1/2,j}(hv)-v_{i+1/2,j}\Delta_{i+1/2,j}h}{c_{i+1/2,j}}$$

with similar expressions for the α^G_p values and

$$\theta^F_p=\frac{(\alpha^F_p)_{I+1/2,j}}{(\alpha^F_p)_{i+1/2,j}},\quad I=\begin{cases} i-1 & \text{if } \lambda^F_p>0,\\ i+1 & \text{if } \lambda^F_p<0,\end{cases}\quad v^F_p=\frac{\Delta t}{\Delta x}\lambda^F_p \tag{44}$$

For the complete geometrical source term discretization associated with the (i,j) cell

$$\mathbf{R}^1_{ij}=\mathbf{R}^{1-}_{i+1/2,j}+\mathbf{R}^{1+}_{i-1/2,j},\quad \mathbf{R}^2_{ij}=\mathbf{R}^{2-}_{i,j+1/2}+\mathbf{R}^{2+}_{i,j-1/2} \tag{45}$$

where, for the second-order scheme, following [36],

$$\mathbf{R}^{1\pm}_{i+1/2,j}=\frac{1}{2}\sum_{p=1}^{3}[\beta^F_p\mathbf{r}^F_p(1\pm\operatorname{sgn}(\lambda^F_p)(1-\Phi^F_p(1-|v^F_p|)))]_{i+1/2,j} \tag{46}$$

$$\mathbf{R}^{2\pm}_{i,j+1/2}=\frac{1}{2}\sum_{p=1}^{3}[\beta^G_p\mathbf{r}^G_p(1\pm\operatorname{sgn}(\lambda^G_p)(1-\Phi^G_p(1-|\hat{v}^G_p|)))]_{i,j+1/2} \tag{47}$$

in which $\boldsymbol{\beta}^F_{i+1/2,j}=\mathbf{X}^{-1}_{i+1/2,j}\mathbf{R}_{i+1/2,j}$ and $\boldsymbol{\beta}^G_{i,j+1/2}=\mathbf{X}^{-1}_{i,j+1/2}\mathbf{R}_{i,j+1/2}$, with $\mathbf{R}_{i+1/2,j}$, and $\mathbf{R}_{i,j+1/2}$ being proper discretizations of the source term defined in the next section.

The CFL stability condition in the two-dimensional case gives the calculation of the time step as

$$\Delta t^n = \frac{\min\{\Delta x, \Delta y\} Cr}{\max_{i,j}\{\sqrt{u_{ij}^2 + v_{ij}^2} + c_{ij}\}} \tag{48}$$

When the friction term is present, it is discretized again in a semi-implicit way and the final expression of the numerical scheme becomes [32]

$$\mathbf{Q}_{ij}^{n+1} = \frac{\mathbf{Q}_{ij}^n - \frac{\Delta t^n}{\Delta x}[\mathbf{F}_{i+1/2,j}^n - \mathbf{F}_{i-1/2,j}^n + (\mathbf{R}_{ij}^1)^n] - \frac{\Delta t^n}{\Delta y}[\mathbf{G}_{i,j+1/2}^n - \mathbf{G}_{i,j-1/2}^n + (\mathbf{R}_{ij}^2)^n] + \Delta t^n \theta \mathbf{S}_{ij}^n}{1 - (1-\theta)\Delta t^n \mathbf{S}_{ij}^n / \mathbf{Q}_{ij}^n} \tag{49}$$

8. CONSERVATION PROPERTY AND WET/DRY TREATMENT IN 2D

The extended C-Property and the wet/dry front treatment were presented in [33] only in the one-dimensional case. Here, the ideas presented in Section 4 are extended in two dimensions. Similar work can be found also in References [32, 34]. Consider a flow at rest in 2D, i.e.

$$u(x,y,t) \equiv 0, \quad v(x,y,t) \equiv 0 \quad \text{and} \quad h(x,y,t) = D - B \ \ \forall (x,y,t)$$

where D is a constant. For this case we need to maintain numerically the following flux functions and geometrical source term balance

$$\frac{\partial}{\partial x}\mathbf{F}(\mathbf{q}) + \frac{\partial}{\partial y}\mathbf{G}(\mathbf{q}) = \mathbf{R}(\mathbf{q}, x, y)$$

To obtain this condition numerically, we balance the numerical fluxes with the source term approximations

$$\mathbf{F}_{i+1/2,j} - \mathbf{F}_{i-1/2,j} = \mathbf{R}_{ij}^1 \quad \text{and} \quad \mathbf{G}_{i,j+1/2} - \mathbf{G}_{i,j-1/2} = \mathbf{R}_{ij}^2 \tag{50}$$

In order to take into account wet/dry transitions a natural extension of the C-Property would be that the numerical scheme solves exactly the steady-state solutions of the form

$$u \equiv 0, \quad v \equiv 0, \quad h(x,y) = \begin{cases} D - B(x,y) & \text{if } B < D \\ 0 & \text{else} \end{cases} \tag{51}$$

This solution represents flow at rest when $B(x,y) < D$ and no water elsewhere.

Then we construct redefined discretizations of the source term, by extending the one-dimensional strategy, following the works in [32, 34, 39], as

$$\mathbf{R}_{i+1/2,j}=\begin{cases}\begin{bmatrix}0\\-(c^n_{i+1/2,j})^2h^n_{ij}\\0\end{bmatrix} & \text{if } h^n_{i,j}<B(x_{i+1},y_j)-B(x_i,y_j)\\ \begin{bmatrix}0\\(c^n_{i+1/2,j})^2h^n_{i+1,j}\\0\end{bmatrix} & \text{if } h^n_{i+1,j}<B(x_i,y_j)-B(x_{i+1},y_j)\\ \begin{bmatrix}0\\-(c^n_{i+1/2,j})^2(B(x_{i+1},y_j)-B(x_i,y_j))\\0\end{bmatrix} & \text{in other cases}\end{cases}\tag{52}$$

and

$$\mathbf{R}_{i,j+1/2}=\begin{cases}\begin{bmatrix}0\\0\\-(c^n_{i,j+1/2})^2h^n_{ij}\end{bmatrix} & \text{if } h^n_{i,j}<B(x_i,y_{j+1})-B(x_i,y_j)\\ \begin{bmatrix}0\\0\\(c^n_{i,j+1/2})^2h^n_{i,j+1}\end{bmatrix} & \text{if } h^n_{i,j+1}<B(x_i,y_j)-B(x_i,y_{j+1})\\ \begin{bmatrix}0\\0\\-(c^n_{i,j+1/2})^2(B(x_i,y_{j+1})-B(x_i,y_j))\end{bmatrix} & \text{in other cases}\end{cases}\tag{53}$$

Next, and refereing to Figure 12 for a hypothetical situation, we modify the correction presented in Section 4, for a flow in motion, in order to avoid unphysical overtopping at steps of arbitrary size. The following procedure is proposed here assuming, without loss of generality, that the cell C_{ij} is wet.

- First the modified source terms (52) and (53) are computed.
- We identify on the neighbour cells $C_{i+1,j}$, $C_{i-1,j}$, $C_{i,j+1}$, $C_{i,j-1}$ in order to determine which of them are dry.

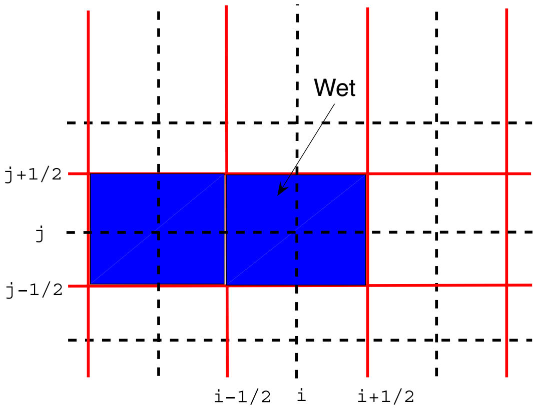

Figure 12. A wet/dry situation in the two-dimensional grid.

- ○ In the case of a neighbour dry cell in the x-direction (i.e. $\mathbf{Q}^n_{i+1,j}=[0,0,0]^{\mathrm{T}}$) we define a new temporary state in the cell C_{ij}

$$\tilde{\mathbf{Q}}^n_{ij}=\begin{bmatrix} h^n_{ij} \\ 0 \\ h^n_{ij}v^n_{ij} \end{bmatrix} \tag{54}$$

  - – We compute the flux $\mathbf{F}^n_{i+1/2,j}$, the source term contribution $\mathbf{R}^{1-}_{i+1/2,j}$ and source term contribution $\mathbf{R}^{1+}_{i+1/2,j}$, associated to the $C_{i+1,j}$ cell, using the values $\tilde{\mathbf{Q}}^n_{ij}$, $\mathbf{Q}^n_{i+1,j}$.
  - – We set the value of $\mathbf{Q}^n_{ij}$ to the one it was before we define the temporary state, in order to correctly compute the flux and source term contribution at the other three interfaces.

- ○ In the case of a neighbour dry cell in the y-direction (say for example cell $C_{i,j+1}$) we define a new temporary state

$$\approx{\mathbf{Q}}^n_{ij}=\begin{bmatrix} h^n_{ij} \\ h^n_{ij}u^n_{ij} \\ 0 \end{bmatrix} \tag{55}$$

  - – We compute the flux $\mathbf{G}^n_{i,j+1/2}$ and $\mathbf{R}^{2\pm}_{i,j+1/2}$ evaluated using the values $\approx{\mathbf{Q}}^n_{ij}$, $\mathbf{Q}^n_{i,j+1}$.
  - – We set the value of $\mathbf{Q}^n_{ij}$ to the one before the temporary state was defined.

- Having completed the procedure at each cell interface, we calculate $\mathbf{Q}^{n+1}_{ij}$.

The procedure is similar in a dry/wet situation. With the above procedure the solution at each wet/dry interface is considered to be that corresponding to an emerging bottom situation for a water at rest and then, in order to compute $\mathbf{Q}^{n+1}_{ij}$, the numerical fluxes corresponding to this approximate solution at the interface are used. In this way the wet/dry front is only allowed to advance when the water gradient in the wet cell is larger than the bottom gradient between cells. The numerical scheme is applied without any modification when no bottom emerge occur.

9. NUMERICAL RESULTS IN 2D

9.1. Test of mass conservation

The aim of this simple numerical test is to verify if mass is preserved when the treatment presented in Section 8 is applied. We consider a channel with rectangular cross section, constant width and length of 40 m. The bed topography is that of a step and is given by

$$B(x,y)=\begin{cases}0 & \text{if } x\in[0,30),\quad y\in[0,40]\\ 0.6 & \text{if } x\in[30,40],\quad y\in[0,40]\end{cases}$$

and a dam is placed at $x=15.5$ m, simulated by the initial conditions

$$h(x,y,0)=\begin{cases}0.4 & \text{if } x\in[0,15.5),\quad y\in[0,40]\\ 0 & \text{if } x\in[15.5,40],\quad y\in[0,40]\end{cases},\qquad u(x,y,0)\equiv 0,\quad v(x,y,0)\equiv 0$$

Solid boundary wall is imposed on the three sides of the channel and along with the presence of the step there are no mass loses through the boundaries; thus, the total mass has to be preserved. Although this test case represents, essentially, a one-dimensional flow in a two-dimensional setting, it can serve as a benchmark problem and important conclusions can be drawn. Yet, the runup of breaking or nonbreaking waves on very steep slopes can be compared to the reflection of an incident wave on a vertical wall.

The numerical scheme was run with $\Delta x=\Delta y=0.8$ and CFL $=0.5$ with the correction presented in Section 8 (for a fluid in motion) and without it. The results in Figure 13, at $t=10$ s, show that the water, wrongly, overtops the step when the correction is not applied. Running the corrected scheme until a steady-state solution, corresponding to water at rest, was reached, the measured final mass error was to the order of 10^{-13}.

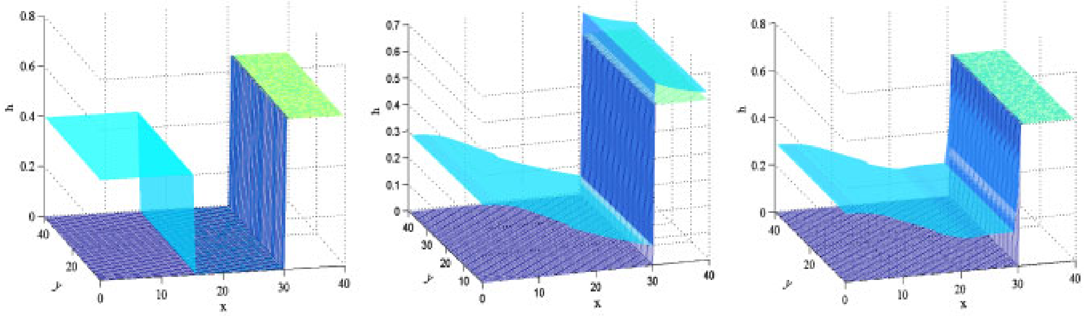

Figure 13. Mass conservation test: initial condition (left), without correction (middle) and with correction (right).

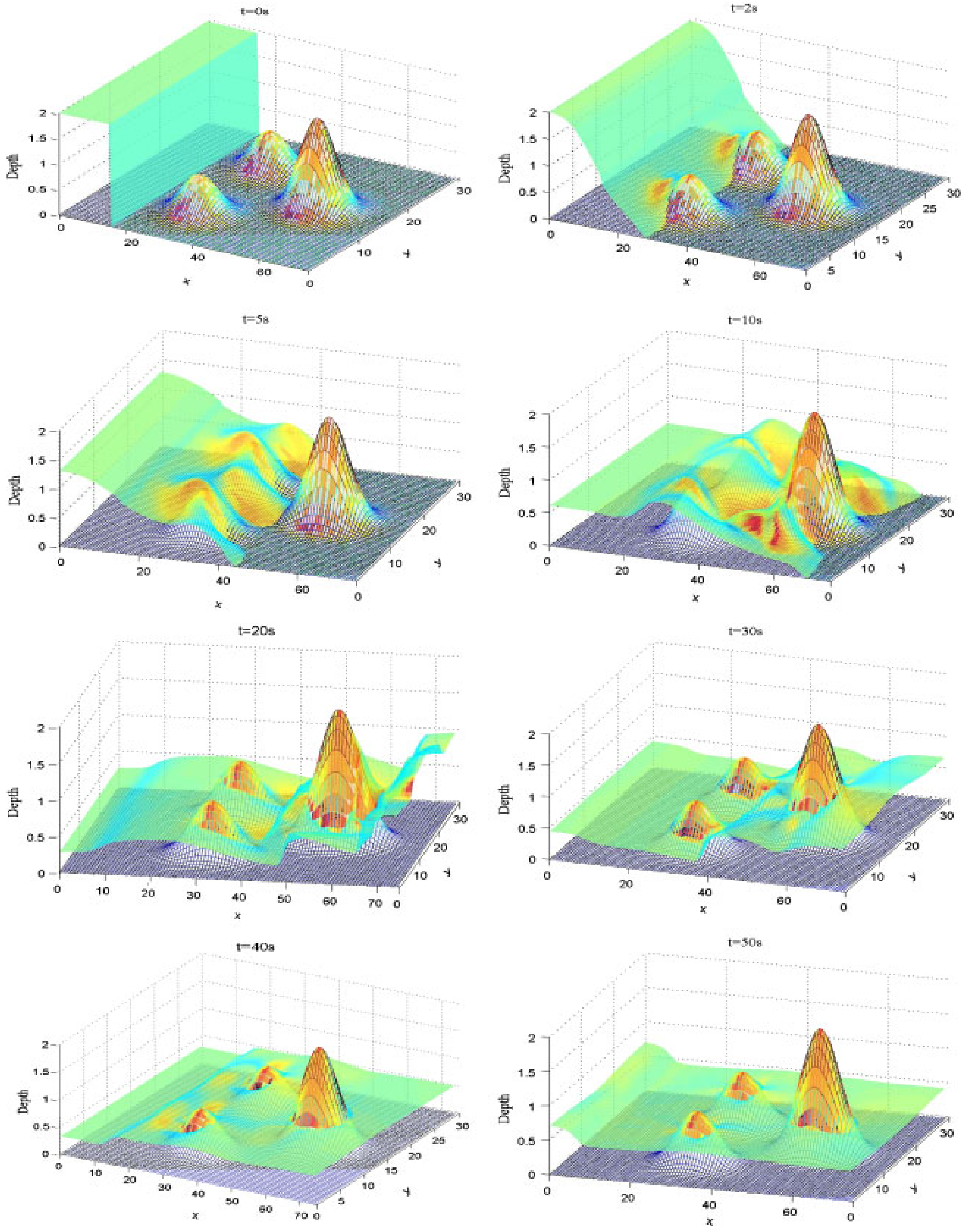

Figure 14. Wetting and drying in a channel: depth evolution.

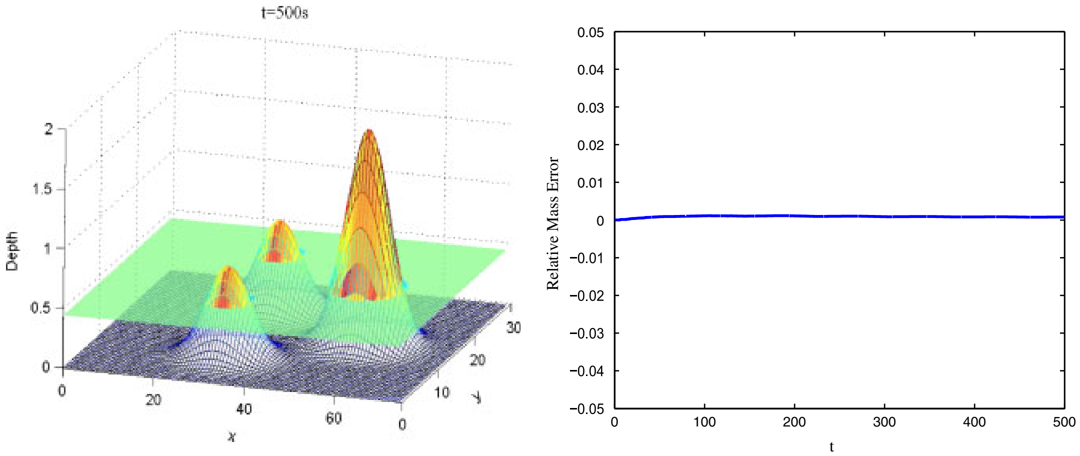

Figure 15. Wetting and drying in a channel: final steady state (left) and mass error history (right).

9.2. Dam-Break in a channel with topography and friction

In this test case, the performance of the presented scheme as to calculate more realistic situations is validated. The problem is similar to that presented in References [34, 40, 41]. This problem, although it does not fit in the long wave framework, can serve as a good numerical test in terms of the wetting/drying process and conservation. In a channel 75 m long and 30 m wide the dam is situated at $x=16$ m with initial water depth $h+B=1.875$ m, while the rest of the channel is considered dry. Three mounds are located in the channel bottom. The initial condition and the channel geometry can be seen in Figure 14 on top left. The Manning coefficient $n_{\mathrm{m}}=0.018$ for this problem. Boundary conditions are for fixed solid walls. A CFL $=0.4$ was used with $\Delta x=0.75$, $\Delta y=0.5$ and $\theta=0.5$ in (49).

Numerical results are presented in Figure 14 for the water movement at different times to show the propagation of the flood until steady state is reached. The small mounds are covered by the water in its propagation and the effect of advancing and recession over the sloppy bed is clear. The higher mound is always almost dry and the accumulation of water can be clearly observed. The collision of the advancing front first with the higher mound and then with the downstream boundary wall can be seen having the expected physical behaviour. The generation of dry bed can also be observed for the small mounds as time evolves until it reaches a steady state. Figure 15 presents this steady state at $t=500$ s along with the evolution of the relative mass error, proving the scheme to be highly conservative.

9.3. Tsunami runup onto a complex three-dimensional beach

In this section, numerical results are compared with the laboratory data produced from a wave tank experiment. This benchmark problem was also proposed in the Third International Workshop on Long-Wave Runup Models. The wave tank was built as a 1:400 scale model approximating the coastline bathymetry near Monai in Japan. This region suffered inundation from the 1993 Okushiri tsunami. A significant feature of this tsunami was a maximum runup of 31.7 m observed at the

DOI: 10.1002/fld

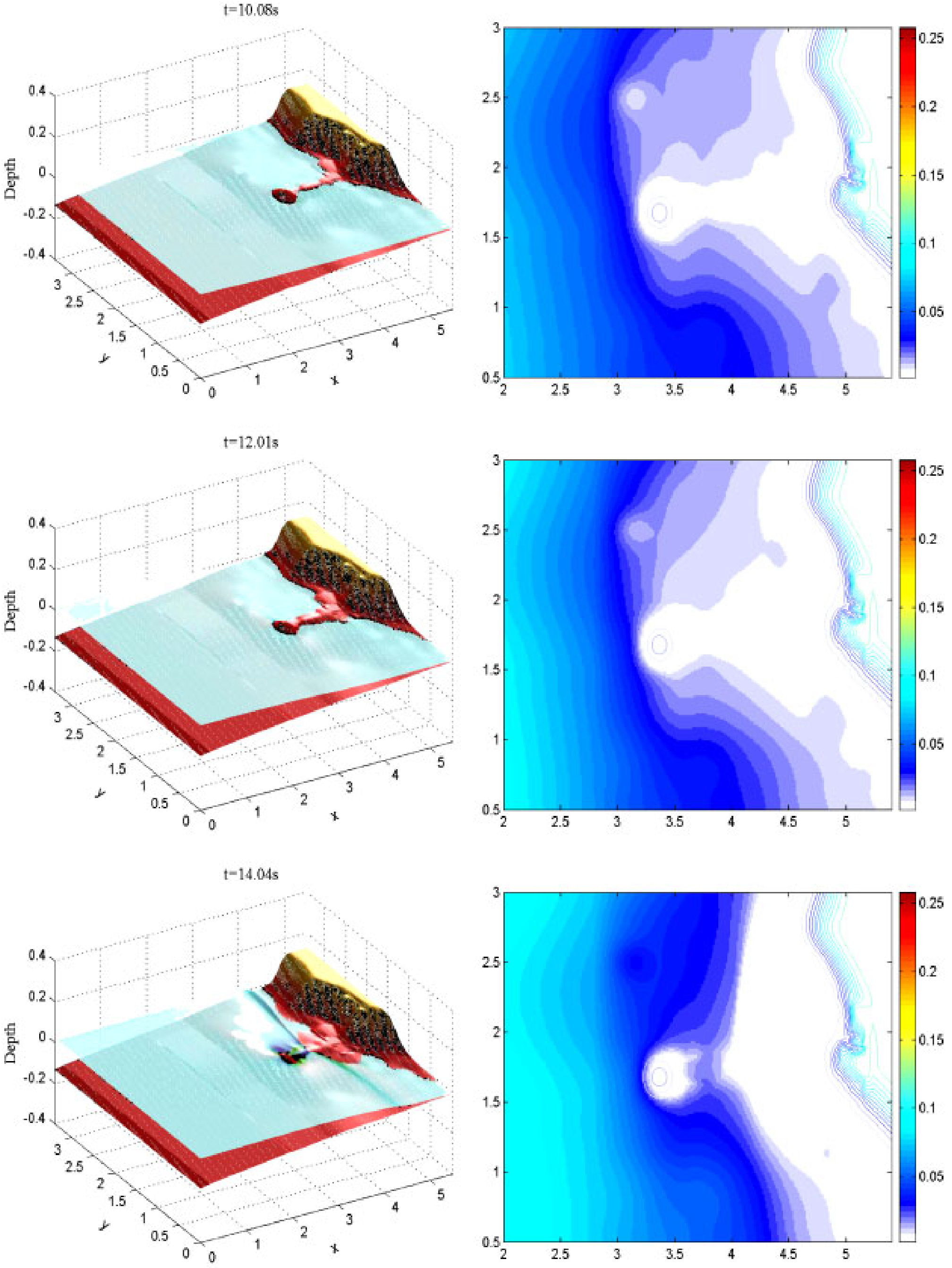

Figure 16. Runup due to the Okushiri tsunami: three-dimensional view (left) and contour view (right) at various times.

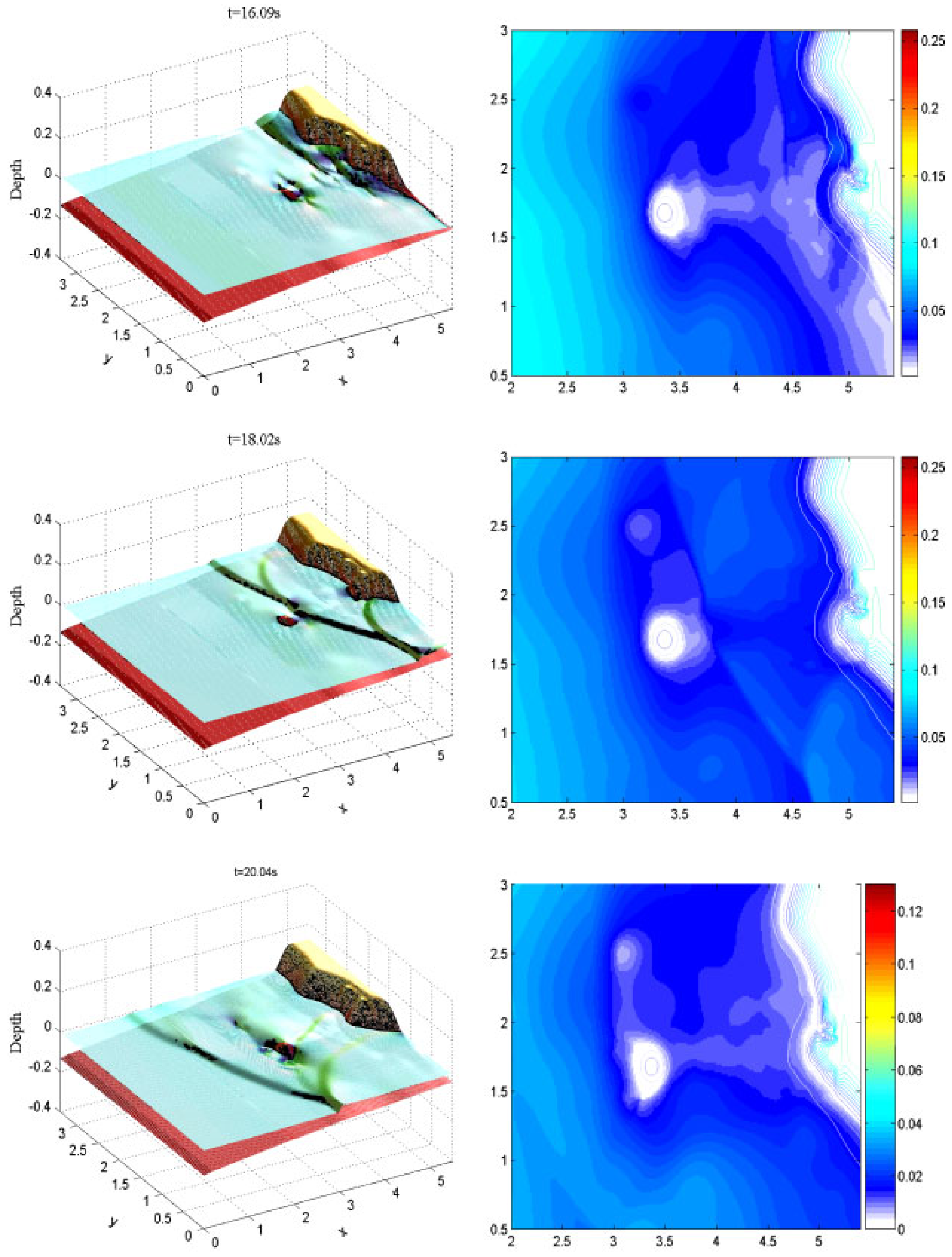

Figure 17. Runup due to the Okushiri tsunami (continued): three-dimensional view (left) and contour view (right) at various times.

DOI: 10.1002/fld

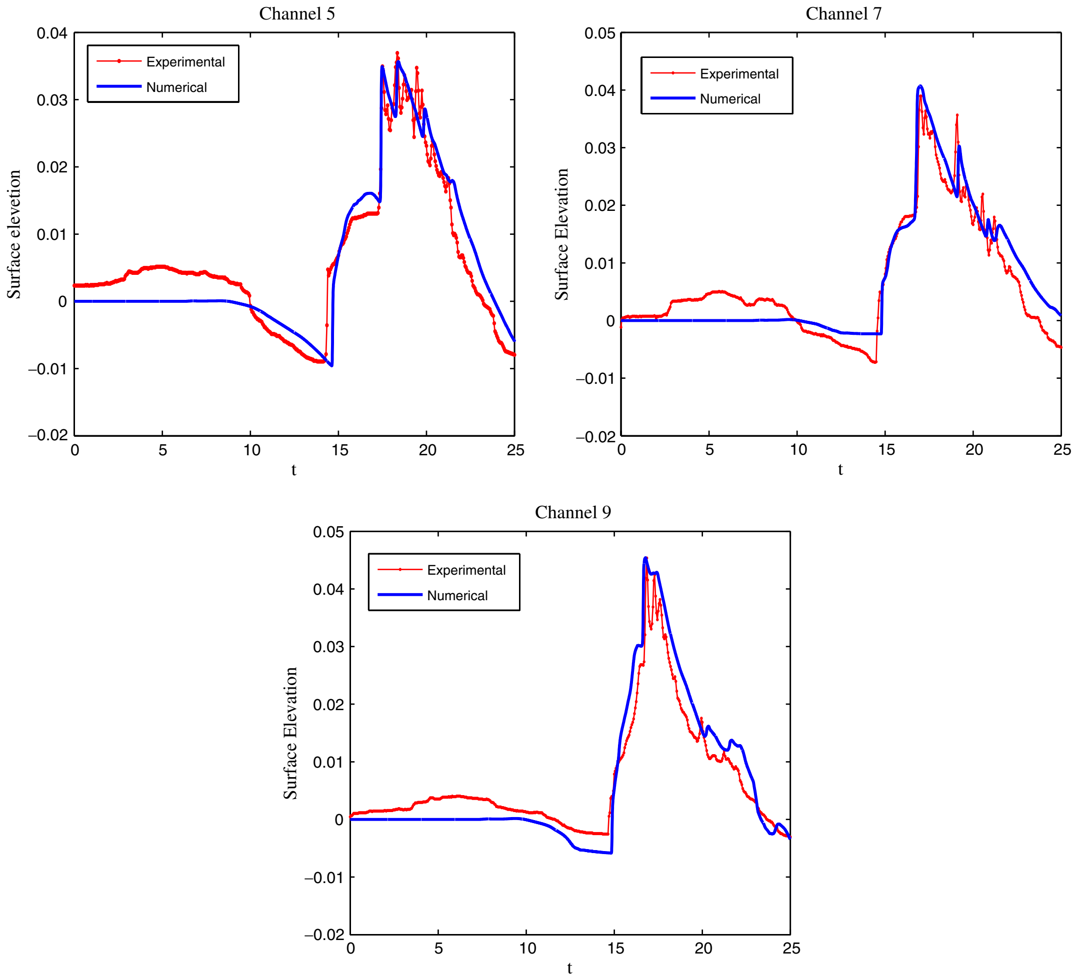

Figure 18. Time variation of the surface level at Channels 5, 7, 9.

head of the Monai Valley, which opens onto a small pocket beach. This runup was not uniform along the coast and is thought to have resulted from a particular topographic effect.

In the experiment, the incoming wave was induced by mechanical wave paddles along one side of the tank and the resulting motion of the surface elevation was measured by gauges at three separate locations. The initial data sets of bathymetry, topography and the wave specifications for this problem, along with the collected data and an overhead movie of the experiment, are available at the workshop website. The computational domain, which models a subregion of the tank, is $(x, y) \in [0, 5.488\,\mathrm{m}] \times [0, 3.402\,\mathrm{m}]$. This include the inlet region that experienced large wave runup. At $x = 0$ and for a time period of $t = [0, 22.5\,\mathrm{s}]$ the provided data specify the measured surface elevation of an incoming wave. The CFL number used for this simulation was 0.4 on a single uniform grid of 392×243 cells with the Manning coefficient equal to 0.025.

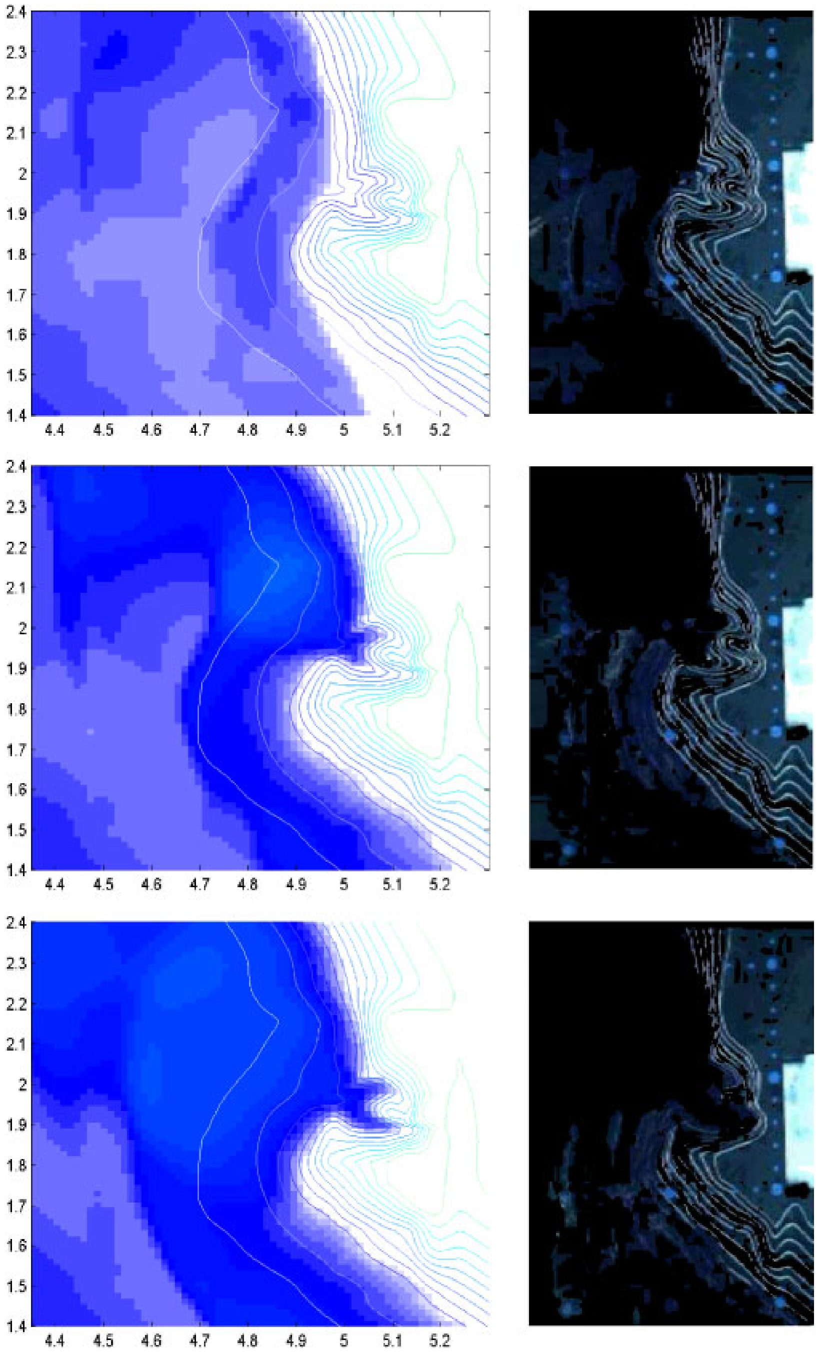

Figure 19. Comparison of numerical solution (left) with snapshots from the overhead movie of the laboratory experiment (right).

The computed surface elevation is shown at various times in Figures 16 and 17 where a three-dimensional view of the computed solution (along with the topography) during the primary runup period is presented. In Figures 16 and 17 contour lines show the topography that was initially above the water surface, including an island. In Figure 16 we can observe that after an initial draw down the tsunami travel towards onshore and that diffracted waves met together behind the island. Then, and in Figure 17, the tsunami wave reaches the land and we can see reflected waves from the coast. A breaking wave is generated by superposition of waves coming from two different coasts, showing the largest value of wave height.

The data sets provided at the workshop also contained water depth series from three wave gauges (denoted Channels 5, 7 and 9) situated offshore from the inundation area and at points $(4.521, 1.196)$, $(4.521, 1696)$ and $(4.521, 2.196)$, respectively. Figure 18 compares the data from the wave tank and the numerical results obtained at the gauges. The plots show good agreement between the three measured time series and the obtained numerical results. At Channel 5 the numerical result models accurately the initial draw down, the wave shoulder and the subsequent reflections. The discrepancy between computed and measured data in the first 10 s is due to the initial condition in the physical tank not being uniformly zero. Nevertheless, the arrival time and the amplitude of the leading waves are correctly computed. Similarly good comparisons are evident with data from the other two gauges.

The maximum computed runup height was about 0.074 m in the numerical model scale, which corresponds to almost 30 m in the prototype scale and thus replicates fairly well the Monay Valley runup and demonstrates its occurrence to be due to the interaction of the tsunami wave with the two small juxtaposed valleys above the coastline. Figure 19 compares the numerical solution with close-up snapshots from the overhead movie produced from the laboratory experiment, demonstrating the similarities in the costal zone where the maximum runup occurred.

10. CONCLUSIONS

In this work, the formulation and validation of a finite volume shock capturing numerical scheme that implements the Roe approximate Riemann solver and a well-known definition of a well-balanced conservation property (the so-called C-Property) were presented in order to investigate the potential to accurately and robustly compute flow regimes related to the propagation and runup of long waves modelled by the nonlinear shallow water (NLSW) equations. A previously introduced improved numerical technique in order to calculate wet/dry fronts over adverse steep slopes in one dimension is applied. This technique is validated and applied here to one and two dimensions and for a second order in space version of the finite volume scheme. Solving the NLSW equations, the resulting scheme provides a reasonably good prediction of general patterns and important characteristics of the runup process. The numerical results agree well with analytical solutions and experimental benchmark data. The presented scheme provided a good approximation of a breaking wave as a propagating bore or a stationary hydraulic jump showing an excellent capability in conserving the mass volume and, although this lead to a slight phase shift of the bore, the solution fully recovered after the breaking process stopped. The numerical results for the maximum runup, the wave profile and the moving shoreline agree quite well with the analytical and experimental data under breaking or nonbreaking conditions. Emphasis was given to recently presented benchmark problems from the Third International Workshop on Long-Wave Runup Models in order to verify and validate the numerical scheme. The numerical

DOI: 10.1002/fld

scheme was proven stable, robust and fairly accurate for problems representing more realistic situations.

REFERENCES

1. Carrier GF, Greenspan HP. Water waves of finite amplitude on a sloaping beach. *Journal of Fluid Mechanics* 1958; **4**:97–109.
2. Thacker WC. Some exact solutions to the nonlinear shallow water wave equations. *Journal of Fluid Mechanics* 1981; **107**:499–508.
3. Synolakis CE. The run up of solitary waves. *Journal of Fluid Mechanics* 1987; **185**:523–545.
4. Liu PL-F, Lynett P, Synolakis CE. Analytical solutions for forced long waves on a sloping beach. *Journal of Fluid Mechanics* 2003; **478**:101–109.
5. Carrier GF, Wu TT, Yeh H. Tsunami run-up and draw-down on a plane beach. *Journal of Fluid Mechanics* 2003; **475**:79–99.
6. Titov VV, Synolakis CE. Modeling of breaking and nonbreaking long-wave evolution and runup using VTCS-2. *Journal of Waterway*, *Port*, *Coastal and Ocean Engineering* 1995; **121**:308–461.
7. Liu PL-F, Cho Y-S, Griggs MJ, Kanoglou U, Synolakis CE. Runup of solitary wave on a circular island. *Journal of Fluid Mechanics* 1995; **302**:259–285.
8. Titov VV, Synolakis CE. Numerical modeling of tidal wave runup. *Journal of Waterway*, *Port*, *Coastal and Ocean Engineering* 1998; **124**:157–171.
9. Li Y, Raichlen F. Non-breaking and breaking solitary wave run-up. *Journal of Fluid Mechanics* 2002; **456**:295–318.
10. Dodd N. Numerical model of wave run-up, overtopping and regeneration. *Journal of Waterway*, *Port*, *Coastal and Ocean Engineering* 1998; **124**:73–81.
11. Hubbard ME, Dodd N. A 2D numerical model of wave runup and overtopping. *Coastal Engineering* 2002; **47**:1–26.
12. Lynett PJ, Wu TR, Liu PL. Modeling wave runup with depth integrated equations. *Coastal Engineering* 2002; **46**:89–107.
13. Hu K, Mingham CG, Causon DM. Numerical simulation of wave overtopping of coastal structures using the non-linear shallow water equations. *Coastal Engineering* 2000; **41**:433–465.
14. LeVeque RJ, George DL. High-resolution finite volume methods for the shallow water equations with bathymetry and dry states. In *Advanced Numerical Models for Simulating Tsunami Waves and Runup*, Yeh H, Liu PL, Synolakis CE (eds). Advances in Coastal and Ocean Engineering, vol. 10. World Scientific Publishing Co.: Singapore, in press.
15. Mader CL. *Numerical Modeling of Water Waves*. CRC Press: Boca Raton, 2004.
16. Imamura F. Review of tsunami simulation with finite difference method. In *Long-Wave Runup Models*, Yeh H, Liu P, Synolakis RC (eds). World Scientific Publishing Co.: Singapore, 1996; 25–42.
17. Bradford SF, Sanders BF. Finite-volume model for shallow-water flooding of arbitary torography. *Journal of Hydraulic Engineering* 2002; **128**:289–298.
18. Brocchini M, Bernetti R, Mancinelli A, Albertini G. An efficient solver for nearshore flows based on the WAF method. *Coastal Engineering* 2001; **43**:105–129.
19. Gopalakrishnan TC, Tung CC. Run-up of non-breaking waves: a finite-element approach. *Coastal Engineering* 1980; **4**:3–32.
20. Zelt JA. The run-up of nonbreaking and breaking solitary waves. *Coastal Engineering* 1991; **15**:205–246.
21. Yeh H, Liu PL, Synolakis CE (eds). *Long Wave Runup Models*. World Scientific Publishing Co.: Singapore, 1996.
22. Helluy P, Golay F, Caltagirone J-P, Lubin P, Vincent S, Drevard D, Marcer R, Fraunie P, Seguin N, Grilli S, Lesage A-C, Dervieux A, Allain O. Numerical simulations of wave breaking. *ESAIM*: *Mathematical Modelling and Numerical Analysis* 2005; **39**(3):591–607.
23. Vincent S, Caltagirone JP, Bonneton P. Numerical modelling of bore propagation and runup on sloping braches using a MacCormack TVD scheme. *Journal of Hydraulic Research* 2001; **39**:41–49.
24. Cea L, Ferreiro A, Vázquez-Cendnó ME, Puertas J. Experimental and numerical analysis of solitary waves generated by bed and boundary movements. *International Journal for Numerical Methods in Fluids* 2004; **46**:793–813.
25. Marche F, Bonneton P, Fabrie P, Seguin N. Evaluation of well-balanced bore-capturing schemes for 2d wetting and drying processes. *International Journal for Numerical Methods in Fluids* 2007; **53**:867–894.

26. Roe PL. Approximate Riemann solvers, parameter vectors, and difference schemes. *Journal of Computational Physics* 1981; **43**:357–372.
27. Bermudez A, Vázquez-Cendón ME. Upwind methods for hyperbolic conservation laws with source terms. *Computers and Fluids* 1994; **23**:1049–1071.
28. Vázquez-Cendón ME. Improved treatment of source terms in upwind schemes for the shallow water equations in channels with irregular geometry. *Journal of Computational Physics* 1999; **148**:497–526.
29. LeVeque RJ. *Finite Volume Methods for Hyperbolic Problems*. Cambridge University Press: Cambridge, 2002.
30. Harten A. High resolution schemes for hyperbolic conservation laws. *Journal of Computational Physics* 1983; **49**:357–393.
31. Delis AI, Skeels CP. TVD schemes for open channel flow. *International Journal for Numerical Methods in Fluids* 1998; **26**:791–809.
32. Brufau P, García-Navarro P, Vázquez-Cendón ME. Zero mass error using unsteady wetting–drying conditions in shallow flows over dry irregular topography. *International Journal for Numerical Methods in Fluids* 2004; **45**:1047–1082.
33. Castro MJ, Ferreiro AM, García-Rodriguez JA, González-Vida JM, Macías J, Parés C, Vázquez-Cendón ME. The numerical treatment of wet/dry fronts in shallow flows: application to one-layer and two-layer systems. *Mathematical and Computer Modelling* 2005; **42**:419–439.
34. Brufau P, Vázquez-Cendón ME, Gracía-Navarro P. A numerical model for the flooding and drying of irregular domain. *International Journal for Numerical Methods in Fluids* 2002; **39**:247–275.
35. Castro MJ, González-Vida JM, Parés C. Numerical treatment of wet/dry fronts in shallow flows with a modified Roe scheme. *Mathematical Models and Methods in Applied Sciences* 2006; **16**:897–931.
36. Hubbard ME, Garcia-Navarro P. Flux difference splitting and the balancing of source terms and flux gradients. *Journal of Computational Physics* 2000; **165**:89–125.
37. Sweby PK. High resolution schemes using flux limiters for hyperbolic conservation laws. *SIAM Journal on Numerical Analysis* 1984; **21**:995–1011.
38. Yeh H, Liu PL, Synolakis CE (eds). *Advanced Numerical Models for Simulating Tsunami Waves and Runup*, Advances in Coastal and Ocean Engineering, vol. 10. World Scientific Publishing Co.: Singapore, in press.
39. Cea L, French JR, Vázquez-Cendón ME. Numerical modelling of tital flows in complex estuaries including turbulance: an unstructured finite volume solver and experimental validation. *International Journal for Numerical Methods in Engineering* 2006; **67**:1909–1932.
40. Brufau P, García-Navarro P. Unsteady free surface flow simulation over complex topography with a multidimensional upwind technique. *Journal of Computational Physics* 2003; **186**:503–526.
41. Delis AI, Katsaounis Th. Numerical solution of the two-dimensional shallow water equations by the application of relaxation methods. *Applied Mathematical Modelling* 2005; **29**:754–783.